REVIEW
SPACE PHYSICS: IONOSPHERE PHYSICS

Earth and Planetary Physics
2: 89–111, 2018
doi: 10.26464/epp2018011

Chinese ionospheric investigations in 2016–2017

LiBo Liu[1,2,3,4*], and WeiXing Wan[1,2,3,4]

[1]Key Laboratory of Earth and Planetary Physics, Institute of Geology and Geophysics, Chinese Academy of Sciences, Beijing 100029, China;

[2]Institutions of Earth Science, Chinese Academy of Sciences, Beijing 100029, China;

[3]Beijing National Observatory of Space Environment, Institute of Geology and Geophysics, Chinese Academy of Sciences, Beijing 100029, China;

[4]College of Earth and Planetary Sciences, University of the Chinese Academy of Sciences, Beijing 100049, China

Abstract: After the release of the previous report to the Committee on Space Research (COSPAR) on progress achieved by Chinese scientists in ionospheric researches (Liu LB and Wan WX, 2016), in the recent two years (2016–2017) many interesting new investigations into various ionospheric related issues have been completed. In this report, about 100 publications are summarized. The topics highlighted are as follows: Ionospheric space weather, ionospheric dynamics, ionospheric climatology and modelling, ionospheric irregularity and scintillation, Global Navigation Satellite System (GNSS) related ionospheric issues and other techniques, and radio wave propagation in the ionosphere. An outstanding feature is that more and more observations from the Meridional Project supported the ionospheric investigations.

Keywords: ionosphere; ionospheric storm; space weather; ionospheric dynamics; irregularity

Citation: Liu, L. B., and Wan, W. X. (2018). Chinese ionospheric investigations in 2016–2017. *Earth Planet. Phys.*, *2*, 89–111. http://doi.org/10.26464/epp2018011

1. Ionospheric Space Weather

The response of the ionosphere to geomagnetic activities is a historic and challenging issue. Active geomagnetic activities drive the ionosphere to deviate severely from its normal state. When the deviation is positive, the event is termed a positive phase storm. Similarly, negative deviation events are termed negative phase storms.

An extreme space weather event in solar cycle 24 was the July 2012 geomagnetic storm, characterized by a long-lasting southward interplanetary magnetic field B_z for about 30 h below −10 nT. Investigations of this storm event have revealed several features and mechanisms. Kuai JW et al. (2017) explored the latitudinal, longitudinal, and altitudinal differences for the July 2012 geomagnetic storm, using multiple instrumental observations, including electron density from ionosondes; total electron content (TEC) from Global Positioning System (GPS), Jason-2, and Gravity Recovery and Climate Experiment (GRACE); and the topside ion concentrations observed by the Defense Meteorological Satellite Program (DMSP) spacecraft to present a comprehensive description of regional differences in the ionospheric response to this event. In the Asian-Australian sector, on 16 July the data indicate an intensive negative storm near longitude ~120°E (as shown in Figure 1). In the topside ionosphere, the negative phase is observed mainly in equatorial regions. The topside and bottomside TEC contribute equally to the depletion in TEC, and the disturbed electric fields also make a reasonable contribution. On 15 July, the positive storm effects are stronger in the Eastside than in the Westside. The topside ionosphere makes a major contribution to the enhancement in TEC for the positive phases, showing the crucial role of the equatorward neutral winds. For the American sector, intensification of the equatorial ionization anomaly is stronger in the west side than in the east side and the strongest feature is present in longitude ~110°W. The joint effects of the disturbed electric fields, composition disturbances, and neutral winds cause complex storm time features. Both the topside ion concentrations and TEC reveal a remarkable hemispheric asymmetry, which results mainly from the asymmetry in neutral winds and composition disturbances.

Zhu QY et al. (2016) investigated the contributions of the bottomside and topside ionosphere to the TEC during the two geomagnetic storms that occurred in September 2005 and December 2006, respectively. Although the absolute changes of the topside TEC were larger than those of the bottomside TEC at low and middle latitudes associated with the larger topside effective ionospheric thickness, the relative changes of the topside TEC to the quiet time reference in these two strong storms were not greater than the changes of the bottomside TEC and N_mF_2, the peak electron density of F_2 layer. Zhong JH et al. (2016b) further investigated the local time, altitudinal, and longitudinal dependence of the topside ionospheric storm effect during both the main and recovery phases of the March 2015 geomagnetic storm. They found that at most longitudes there was a persistent topside TEC depletion that lasted for more than 3 days after the storm main phase.

Lei JH et al. (2016b) collected ionospheric observations from ionosondes, ground-based GPS receivers, Gravity Recovery and Cli-

Correspondence to: L. B. Liu, liul@mail.iggcas.ac.cn
Received 11 FEB 2018; Accepted 01 MAR 2018.
Accepted article online 20 MAR 2018.

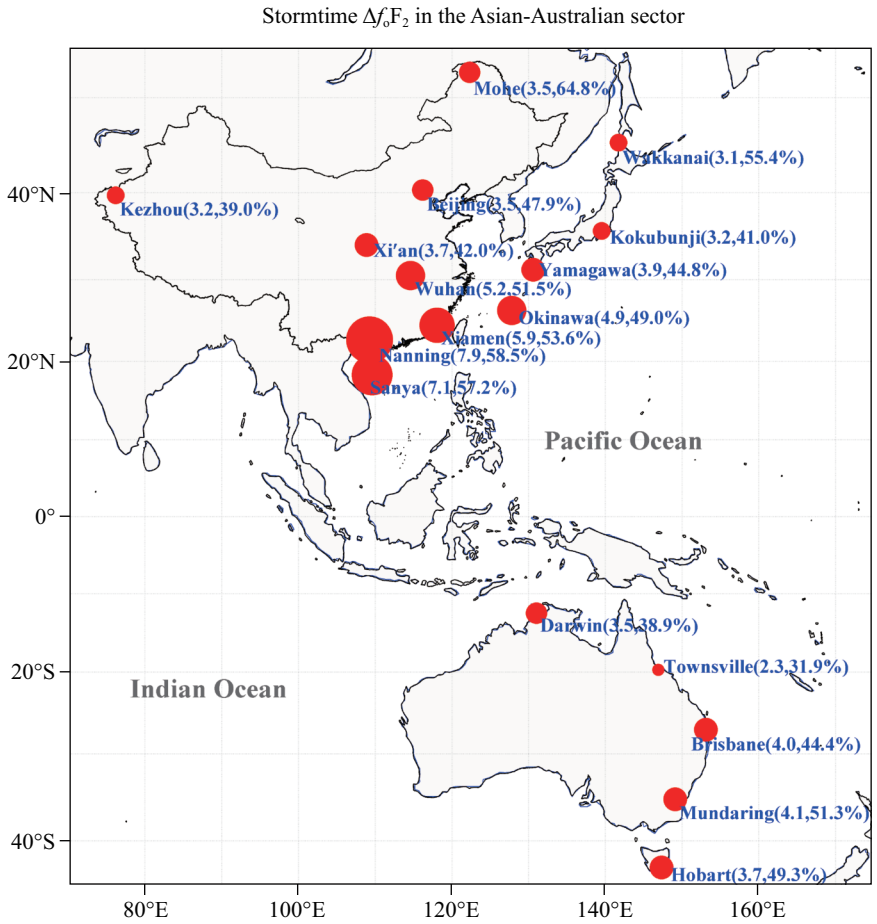

Figure 1. The maximum decrease in the critical frequency of F_2 layer f_oF_2 at 17 stations in the Asian-Australian sector on July 16, showing the latitudinal profile of the notable negative storm. The sizes of the dots are proportional to the peak declining value in f_oF_2. The decline of f_oF_2 (in MHz) and the percentage of the relative decline in f_oF_2 (compared with the geomagnetically quiet conditions) are given in the brackets. After Kuai JW et al. (2017).

mate Experiment (GRACE) and MetOp-A satellites, and Fabry-Perot interferometer over the Asian-Australian sector to investigate the responses of the F_2 peak and the topside ionosphere to the 2 October 2013 geomagnetic storm. Comparisons among the multiple simultaneous observations revealed a contrasting behavior of the topside ionosphere and the F_2 peak in East Asia during the recovery phase of the storm. The upward looking TEC from low-Earth orbit satellites did not undergo such depletions as seen in the region near the F_2 peak, and even showed enhancements. The contrasting behaviors of the F_2 peak and the topside ionosphere is mainly associated with the enhancement of the equatorward winds. Ren DX and Lei JH (2017) further studied the equatorial ionospheric response at Sao Luis (2.5°S, 44.2°W; 6.68°S dip latitude) to the October 2013 geomagnetic storm. The changes of the F_2 peak height (h_mF_2) at the magnetic equator were generally attributed to variations of vertical drift associated with zonal electric fields. They pointed out that, besides vertical drifts, meridional winds and neutral temperature also contributed to the increase of the storm time h_mF_2 at the magnetic equator.

The March 2015 geomagnetic storm is another extreme space weather event that occurred in the current 24th solar cycle. The SYM-H index indicates that the March 2015 storm reached a minimum value of –233 nT. Kuai JW et al. (2016) investigated the ionospheric disturbances over equatorial and low latitudes in the Asian-Australian and American sectors during this event. They explored the evolution of the ionosphere and the essential role that disturbed electric fields played in the ionosphere. Disturbed electric fields comprise penetration electric fields (PEFs) and Disturbance dynamo electric fields (DDEFs). PEFs occur on 17 March in both the American sector and the Asian-Australian sector. The effects of DDEFs are also remarkable in these two longitudinal sectors. As shown in Figure 2, both the DDEFs and PEFs show a notable local time dependence, which causes the sector differences in the characteristics of disturbed electric fields. Local time differences in disturbed electric fields would further lead to sector differences in the low-latitude ionospheric response during this storm. An outstanding feature is that the negative storm effects caused by long-duration DDEFs are intense over the Asian-Australian sector, while the repeated elevations of h_mF_2 and the equatorial ionization anomaly (EIA) intensifications caused by the multiple strong PEFs are more distinctive over the American sector. Especially, the storm time F_3 layer is caught on 17 March in the American equatorial region, proving the effects of the multiple strong eastward PEFs.

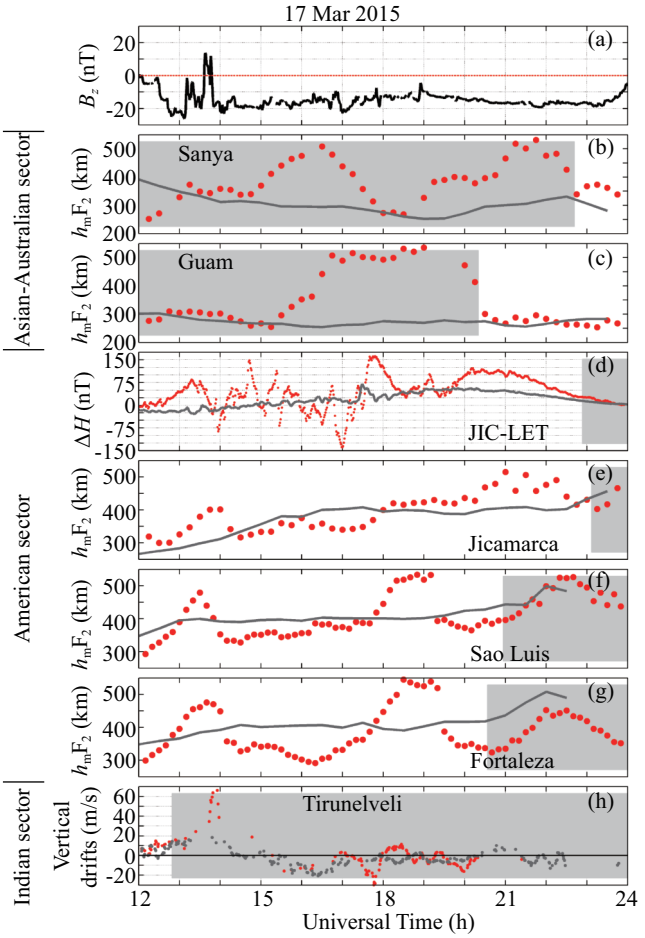

Figure 2. The variations of (a) IMF B_z; (b and c) h_mF_2 at Sanya (18.3°N, 109.6°E; dip latitude 13°N) and at Guam (Asian-Australian Sector); (d) $\Delta H_{jic\text{-}let}$; (e–g) h_mF_2 at Jicamarca, Sao Luis, and Fortaleza (American Sector); and (h) the vertical Doppler drifts at Tirunelveli (Indian Sector) during 12: 00–24: 00 UT of 17 March. The gray curves denote the quiet time reference values of these parameters. The shaded areas indicate the period within 18: 00–06: 00 LT for each station. After Kuai JW et al. (2016).

Jiang CH et al. (2017b) analyzed the equatorial and low-latitude ionospheric response to the March 2015 storm over the Southeast Asia longitude sector. Based on the observations from ionosondes and Swarm satellite, they found that vertical downward transport of plasma or neutrals induced by traveling ionospheric disturbances (TIDs) or traveling atmospheric disturbances (TADs) might make a contribution to the short-term ionospheric positive effect in the main phase of this great storm. The occurrence of daytime spread F at low latitudes might be due to the diffusion of equatorial ionospheric irregularities in the topside ionosphere along geomagnetic field lines.

Jiang CH et al. (2016c) presented the observed daytime spread F that lasted for more than 2 h on 14 November 2015 by using the ionosonde installed at Puer (22.7°N, 101.05°E). They found that TIDs occurred ahead of the daytime spread F occurrence. The downward vertical wind induced by TIDs/atmospheric gravity waves might have a profound effect on the generation of daytime spread F during a geomagnetic storm.

Zhang RL et al. (2017b) analyzed the disturbance plasma drifts triggered by the long-lasting southward Interplanetary Magnetic Field (IMF) B_z. Some common features during the three storms suggest that the disturbance plasma drifts are dominated by the disturbance dynamo. The newly formed disturbance plasma drifts are upward and westward at night, and downward and eastward during daytime. The disturbance plasma drifts evolved with significant local time shifts, gradually migrating from nightside to dayside. The dayside downward disturbance plasma drifts become enhanced and shift to later local times. The local time shifts in disturbance plasma drifts are attributed mainly to the evolution of the disturbance winds. The strong disturbance winds arising around midnight can constantly corotate to later local time. At dayside the westward and equatorward disturbance winds can drive the F region dynamo to produce the poleward and westward polarization electric fields.

Using NCAR Thermosphere Ionosphere Electrodynamics General Circulation Model (TIEGCM) simulations, Chen XT et al. (2016) further investigated the ionospheric response to the 28–29 October 2003 geomagnetic storms. The controlled simulation experiments showed that the storm-time travelling atmospheric disturbances (TADs) triggered by Joule heating could significantly disturb the ionosphere at mid-low latitudes, while the equatorial ionosphere was dominated by the electric fields. Even though the geomagnetic activity was weak, TADs originated in the polar regions could propagate to the opposite hemisphere.

It is always hard to identify the global large scale ionospheric response to disturbances in a consistent way. Fortunately, data assimilation techniques offer us a unique opportunity to combine different sources of data in a unified way to generate global gridded electron density (Figure 3). Based on slant TEC observations made by ~10 satellites and ~450 ground IGS GNSS stations, Yue XA et al., (2016b) constructed a 4-D reanalysis of the ionospheric electron density during the March 17, 2013 geomagnetic storm. Their work identified four main large-scale ionospheric disturbances: (1) the positive storm during the initial phase; (2) the SED (storm enhanced density) structure in both northern and southern hemisphere; (3) the large positive storm in main phase; and (4) the significant negative storm in middle and low latitude during recovery phase. The results were compared with model simulations to identify main drivers of these large scale disturbances.

Ionospheric responses to solar flares were generally focused on the ionospheric effects of photoionization caused by the increased X-rays and extreme ultraviolet irradiance. Little attention was paid to the related electrodynamics. Zhang RL et al. (2017a) explored the equatorial electric field (EEF) and electrojet (EEJ) in the ionosphere at Jicamarca during flares from 1998 to 2008. Their work reveals a negative correlation between EEJ and EEF during solar flares, an increased EEJ and a decreased EEF (Figure 4). During flares, the decreased EEF weakens the equatorial fountain effect and depresses the low-latitude electron density. The enhancement in Cowling conductivity may modulate the ionospheric dynamo and decrease the EEF.

Understanding how the ionosphere responds to extreme space weather events is of great value for applications. Le HJ et al.

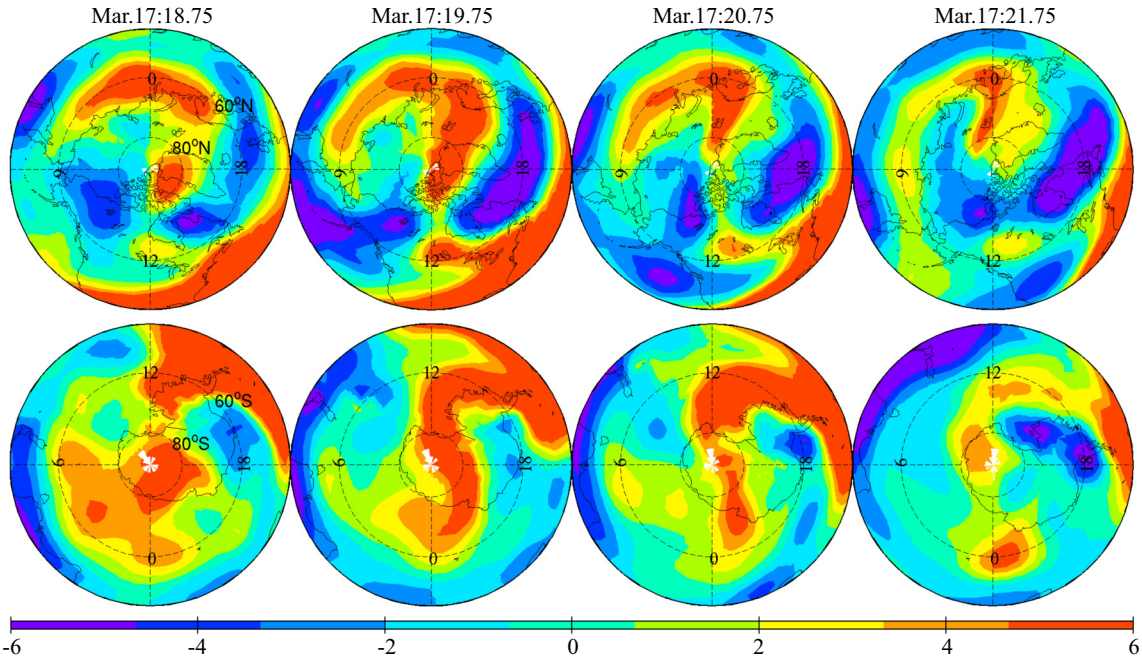

Figure 3. Differential TEC map of data assimilation results with 1-hour interval from the view of North Pole (top panels) and South Pole (bottom panels), respectively. The coordinate system is magnetic local time and magnetic latitude. The date and universal time in hours for each case is given at the top of individual panel. The unit is in TEC unit (TECU, 1 TECU=10^{16}el/m^2). After Yue XA et al. (2016b).

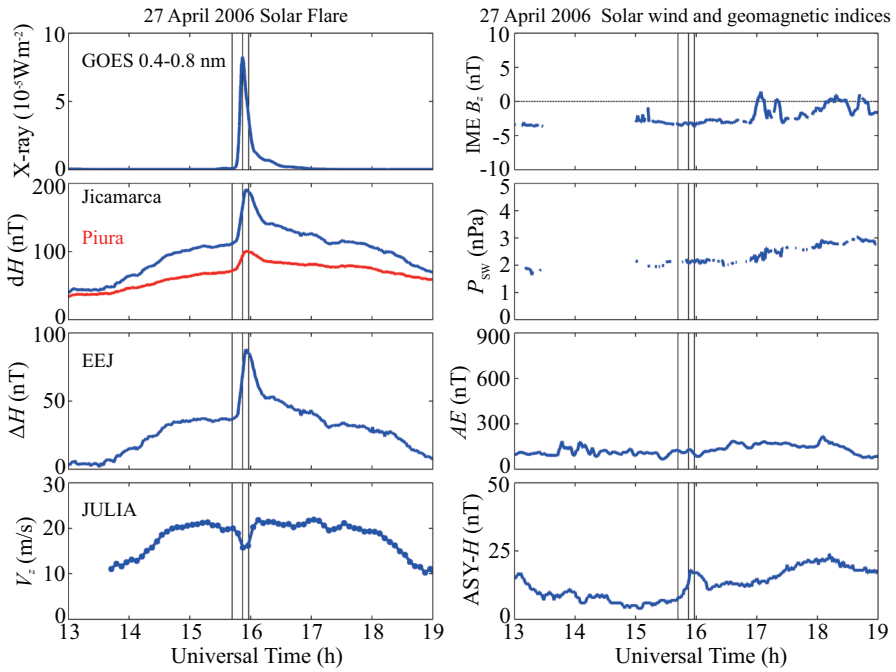

Figure 4. The X-ray fluxes (0.1–0.8 nm) observed by GOES, scaled geomagnetic *H* component at Jicamarca (11.92°S, 78.87°W) and Piura (5.18°S, 80.64°W), equatorial electrojet (EEJ), averaged 150 km vertical drift observed by JULIA, interplanetary magnetic field (IMF) B_z, solar wind dynamic pressure (P_{SW}), *AE* index, and asymmetric ring current (ASY-*H*) index during the 27 April 2006 solar flare. The vertical black lines in each panel from left to right show the start, peak, and end time of the flare, respectively. After Zhang RL et al. (2017a).

(2016a) simulated ionospheric and thermospheric responses to an extreme solar flare of X40. They employed a thermosphere and ionosphere coupling model to conduct several numerical experiments for different classes of solar flares. The responses at high altitudes show a significant amplification effect with increasing flare level. The extreme flare causes huge disturbances in the thermosphere and more than 4 h of ionospheric disturbance, much longer than the responses to normal flares.

Zhang XF et al. (2017) statistically determined the climatology of thermospheric zonal winds under quiet and active geomagnetic

conditions. Measurements of zonal winds from the CHAllenging Minisatellite Payload (CHAMP) exhibit a dependence of the global thermosphere on solar activity. Increases in solar flux enhance eastward winds at low latitudes from dusk to midnight. Storm-induced subauroral westward disturbed jets are stronger during the summer and in the Northern Hemisphere in equinoxes.

Since the ionosphere is significantly dominated by solar and geomagnetic activity, it is very difficult to isolate and study effects on the ionosphere driven by such geophysical phenomena as earthquakes, typhoons, and tropical cyclones. Chen Z et al. (2017a, b) used the spectral whitening method (SWM) to extract the effects of such geomagnetic activity on TEC. Their analysis shows that the SWM can clean up background variations in TEC and effectively extract effects of geomagnetic activity. Their work indicates that SWM may be a potential method to study the ionospheric effects of some weak geophysical driving sources. Based on successful application of SWM to f_oF_2, Chen Z et al. (2017b) used SWM to process TEC. By analyzing the spatial correlation of the disturbance field with $F_{10.7}$ and *Ap*, their work illustrates that SWM can significantly reduce the effects of solar activity and enhance those of geomagnetic activity (as shown in Figure 5). It suggests that the SWM is more effective than traditional methods in extracting effects of geomagnetic activity from TEC. The relative deviation of TEC derived by SWM is more sensitive to geomagnetic activity than solar activity.

Yang N et al. (2016) used ion density data from DMSP and DEMETER (French Detection of Electro-Magnetic Emissions Transmitted from Earthquake Regions) satellites to investigate statistically the location of the mid-latitude ionospheric trough as a function of geomagnetic storm time, in terms of the category and the intensity of storms. The trough is found to move equatorward as the D_{st} index decreases, and poleward as the D_{st} index increases. Compared with the ICME, MC and CIR storms, in sheath storms the trough shifts to lower latitudes at the end of the main phase, although the average storm intensity is weak. For moderate CIR storms, the trough position rapidly recovers at the start of the recovery phase.

Ouyang XY et al. (2016) studied the Ultra-Low-Frequency (ULF) waves induced during the Storm Sudden Commencement (SSC) on March 8th, 2012 using the data from the ground-based magnetometers at the middle and low latitudes, as well as the HF Doppler sounder. In this study, they found a link between ULF waves and ionospheric Doppler shifts. ULF waves in the Pc 1–2 range are observed immediately after the SSC from the ground stations of L-shell ranging from 1.06 to 2.31, which maps to the topside ionosphere. The power spectra of the ionospheric Doppler shift show a weak response in the Pc 1–2 range. In addition, there are a bulge and wavelike structure in the time serials of the ionospheric Doppler shift during this period. The wavelike structure has a clear Pc 3–4 period and correlates well with the magnetic field oscillations observed by the ground-based magnetometers. These results

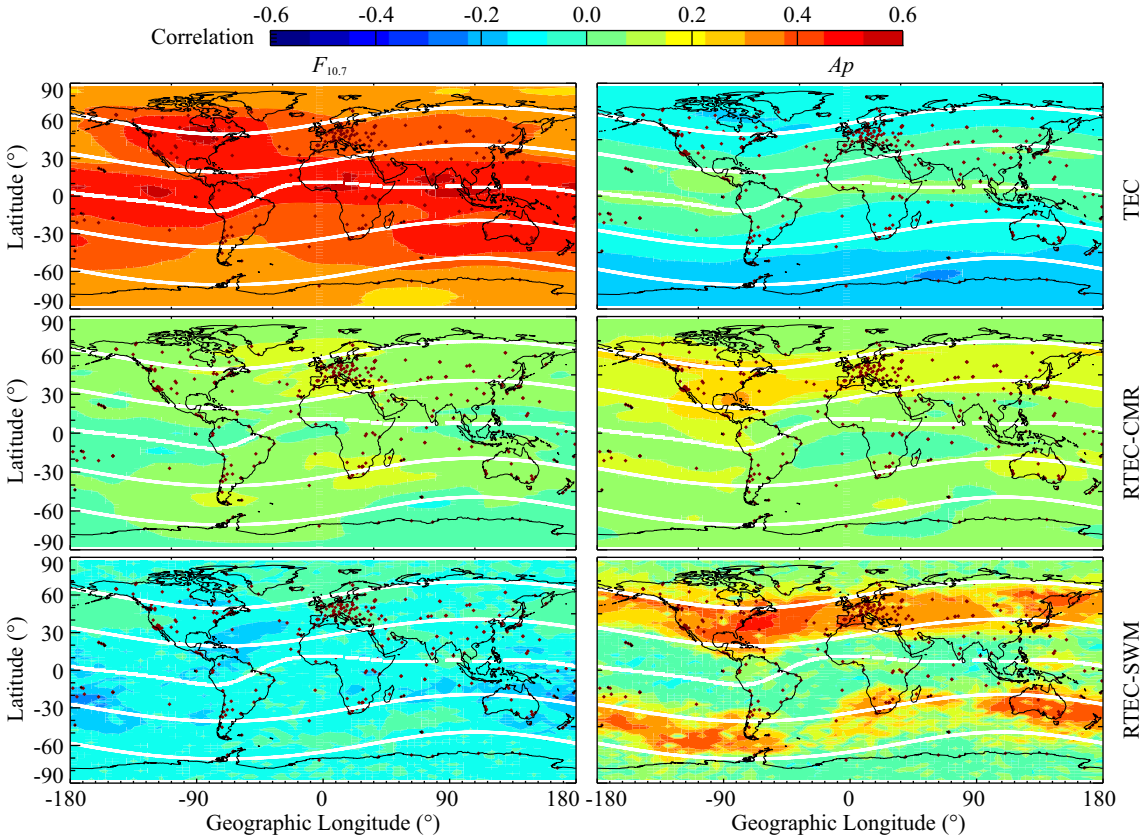

Figure 5. Left Column: The Spatial Correlation (SC) (top row) between $F_{10.7}$ index and TEC, and (middle and bottom rows) between $F_{10.7}$ and RTEC. Right Column: The SC (top row) between *Ap* index and TEC, and (middle and bottom rows) between *Ap* and relative TEC (RTEC). White lines in each image denote geomagnetic latitudes. After Chen Z et al. (2017b).

suggest that ionospheric Doppler shifts can response effectively to ULF waves in various frequency ranges, especially Pc 3–4 and below. This study provides new evidence that ULF waves induced during SSC can propagate into the low-latitude ionosphere.

2. Ionospheric Dynamics

Zhang RL et al. (2015) statistically presented the dawn enhancement of the equatorial ionospheric vertical plasma drift in a way similar to the prereversal enhancement based on the satellite observations. It is still not clear whether the signature of such sunrise enhancement appears in observations with other sounding techniques. Zhang RL et al. (2016) explored Jicamarca (12°S, 283.2°E) incoherent scatter radar measurements to verify the evidence of sunrise enhancement in vertical plasma drift on 12 May and 10 June 2004, times of magnetically quiet and solar minimum conditions. The effects of the sunrise enhancement on the ionosphere are investigated by using the ionograms recorded by the Digisonde Portable Sounder at Jicamarca and conducting the Theoretical Ionospheric Model of the Earth in Institute of Geology and Geophysics, Chinese Academy of Sciences. They find that, during the sunrise enhancement, the F_2 layer peak height moves upward remarkably, and the F_2 layer peak density and bottomside electron density tend to decrease compared to the days without sunrise enhancements (Figure 6). The simulations indicated that the sunrise enhancement in drifts can drive the equatorial ionosphere to higher heights and distort the equatorial electron density profiles to form an F_3 layer in the equatorial F region, and a new F_2 layer develops at lower altitudes under the joint control of the usual photochemical and dynamical processes.

Gong Y et al. (2016a) presented a direct comparison of the vertical electric fields in the E- and F-region at Arecibo. They verified the electric field mapping by comparing the E- and F-regions' eastward ion drifts at heights where the E-region vertical ion drift is zero. The results show that the F-region eastward $\boldsymbol{E}\times\boldsymbol{B}$ ion drift and the E-region eastward ion drift at locations where vertical ion drift equals to zero are not consistent. The inconsistency implies that the E-region vertical electric field is not the same as that of the F-region.

He F et al. (2017) presented multi-satellite observations of the evolution of subauroral polarization streams (SAPS) during intense storms (ISs) and quiet time substorms (QSs). They analyzed SAPS that occurred during 37 ISs and 30 QSs. Generally, SAPS occur after the southward turning of the interplanetary magnetic field (IMF), with time lags of 0–1.5 h for ISs and 0–2.5 h for QSs. SAPS usually occurs 0–3 h after the beginning of storm main phases and 0–2 h after the onset of substorm expansions. The lifetimes of SAPS are generally longer than the durations of southward IMF and storm main phases. No SAPS occur during the recovery phases of ISs if IMF keeps northward. During QSs, the lifetimes of SAPS are shorter than the duration of the QSs. Superposed epoch analysis shows different evolution patterns of SAPS during ISs and QSs. Most of the SAPS are seen first before 20: 00 MLT during ISs, with the occurrence maximized around 18: 00

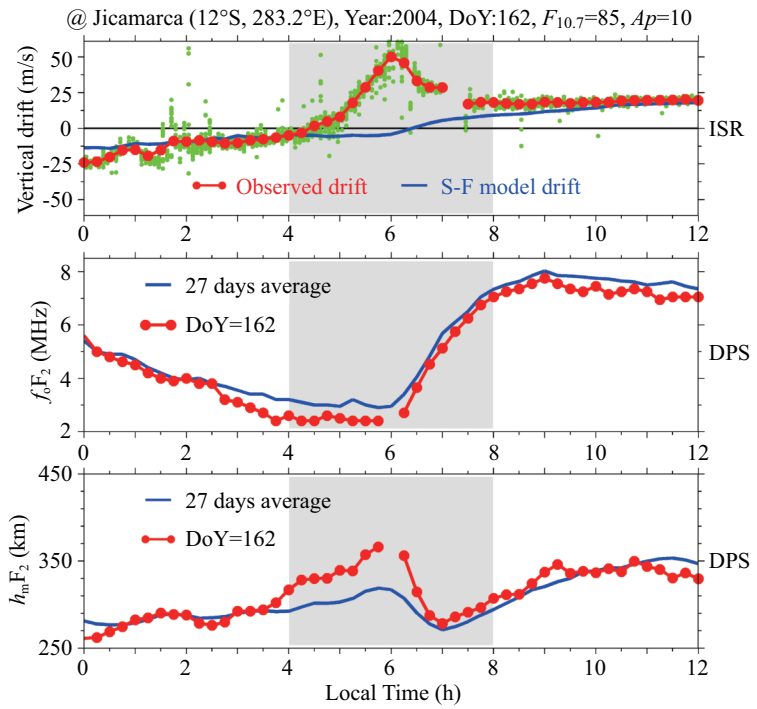

Figure 6. Top: The F region vertical plasma drifts at Jicamarca (12°S, 283.2°E) on 10 June 2004. The green points denote the vertical drifts observed with incoherent scatter radar at heights from 200 km to 450 km, and the red line with dots represents the moving 15 min height-averaged values. The S-F model-predicted drifts are plotted with blue line as a reference. The daily values of $F_{10.7}$ and Ap indices are also marked. Middle and Bottom: The red lines with dots exhibit the ionosonde f_oF_2 and h_mF_2 at Jicamarca on 10 June 2004. The corresponding 27-day average patterns are displayed with blue lines as a reference. The gray areas between 04: 00 and 08: 00 LT show the periods with a sunrise enhancement in vertical drifts. After Zhang RL et al. (2016).

MLT, whereas for QSs most of them appear first after the 19: 00 MLT sector, with the occurrence maximized around 21: 00 MLT. Such a difference might be related to the different current systems that build up in the magnetosphere and ionosphere system for ISs and QSs. Their results provide both physical insight and constraints to modeling the coupling of the magnetosphere-ionosphere-thermosphere system.

He F et al. (2016) reported the double-peak subauroral ion drifts (DSAIDs), which are a unique subset of subauroral ion drifts (SAIDs). Case studies and statistical analyses both show that the two velocity peaks of DSAIDs are associated with two ion temperature peaks and two region-2 field-aligned current Peaks (R2-FACs) in the midlatitude ionospheric trough (MIT), which is located in the low-conductance subauroral region. DSAIDs are regional and vary significantly with magnetic local time. DSAIDs can evolve from/to SAIDs during their lifetimes, which cover from several minutes to tens of minutes. It is also found that DSAIDs occur under conditions more disturbed than those of SAIDs. The generation mechanism of DSAIDs shown in Figure 7 suggests that the various structures (e.g., auroral boundary, MIT, FACs, and temperature peaks) existing in the subauroral region are highly coupled and that the R2-FACs are the essential driver of the westward ion drifts or poleward electric fields.

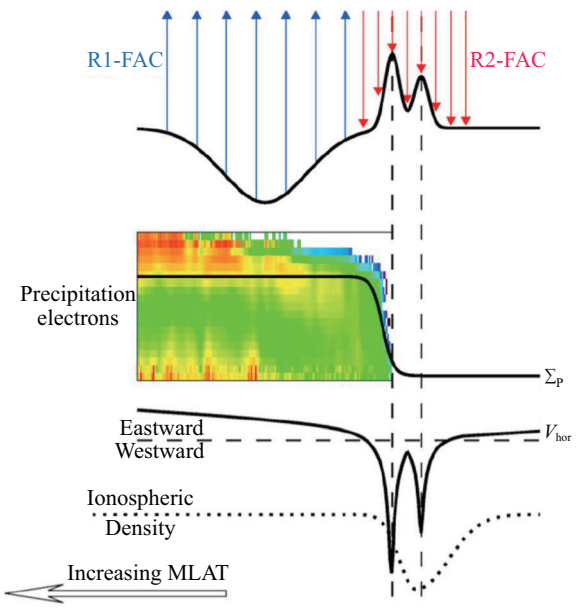

Figure 7. A schematic plot of the production mechanism of DSAIDs associated with FACs (solid arrows), precipitation electrons, height-integrated Pedersen conductance (Σ_P), horizontal ion drift velocity (V_{hor}), and ionospheric electron densities (dotted line). The two westward ion drift peaks of the DSAIDs are marked by the two vertical dashed lines. R1-FAC denotes upward region-1 FACs, and R2-FAC denotes downward region-2 FACs. After He F et al. (2016).

Neutral winds are an important ionospheric dynamical driver. Yu T et al. (2016) used wind data observed by a Fabry-Perot interferometer (FPI) and a meteor radar (MR) to study wind climatology in mesosphere/lower thermosphere over central China and made comparisons between the measurements. A 4-year data series yielded a general similarity in the wind morphology between the FPI winds and MR winds. The study found a stronger correlation coefficient of FPI/MR winds for meridional winds than for zonal winds, and stronger at 87 km than at 97 km. Their work also explored the influence of airglow layer variation on FPI winds.

Coupling between the ionosphere and underlying atmospheric activities is found to be a main source of the ionospheric variability. Typical activities may come from gravity waves, tides, and other waves of lower atmospheric origin.

Yu SM et al. (2016a) used the 12-year (2001 to 2012) GPS TEC data to study the longitudinal difference of medium-scale ttravelling ionospheric disturbance (MSTID) activity at two Chinese stations, CHAN (43.8°N, 125.3°E) and URUM (43.7°N, 87.6°E). The occurrence of MSTIDs depends on local time, season, and solar cycle, and is more frequent at CHAN than at URUM. These features are in full accordance with the occurrences of Spread-F phenomena at the two stations. This study is significant for providing new observational evidence that acoustic gravity waves (AGW), manifested in travelling ionospheric disturbances (TIDs), play an important seeding role in triggering mid-latitude Spread-F in the overhead ionosphere.

Statistical analyses of airglow images and Global Positioning System (GPS) data over central China during 2013–2015 were conducted by Huang FQ et al. (2016) to investigate MSTIDs. The phase fronts of perturbations are aligned from northwest to southeast and propagate toward the southwest. The characteristics of the MSTIDs observed by OI 630.0 nm images are consistent with those from the GPS data. The phase velocities, periods, wavelengths, and amplitudes of MSTIDs are determined from 630.0 nm images and GPS data. Simultaneous observations from OI 630.0 nm and OI 557.7 nm images were used to explore the relationship between MSTIDs and gravity waves (<100 km) in the mesopause. It is found that the nighttime MSTIDs frequently occurred in the summer solstice, which was not consistent with the occurrence of gravity waves observed in the mesopause. The authors pointed out that nighttime MSTIDs may be generated by the coupling of electrodynamic processes rather than being triggered by gravity waves from the lower atmosphere.

MSTIDs may also be triggered by typhoons. Song Q et al. (2017) identified two MSTIDs (on 19 July and 23 July 2014, respectively) during the landing phases of Typhoons Rammasun and Matmo. The MSTIDs excited by Rammasum were detected at 06: 56–07: 40 UT on 19 July 2014, with a mean horizontal phase velocity of 118 m/s and horizontal extension of about 600 km. The Matmo-related MSTIDs were observed at 14: 48–15: 54 UT on 23 July 2014. Both MSTIDs propagated less than 200 km southwestward. The short propagation distances of these MSTIDs suggest that they may have been caused by the body forces resulting from the typhoons.

Chen G et al. (2016a) described ionospheric disturbances in eight locations on the meridional chain from 30.5°N to 42.8°N in northern China during the 2013 sudden stratospheric warming (SSW) event. The midlatitude ionosphere responded strongly to the SSW despite being under high solar flux. The F_2 layer maximum electric density increased by more than 80%, and the peak height was

elevated more than 60 km. Semidiurnal variations were recorded in early and middle January during the SSW. Quasi-16 day planetary wave-like oscillations were observed during the warming event. The coupling between the atmosphere and ionosphere may be strengthened by the quasi-16 day waves.

Liu HT et al. (2017) carried out a detailed observation of the coseismic ionospheric disturbances (CIDs) after the M_w 7.8 Gorkha earthquake by using TEC data from 333 GPS stations. This inland earthquake occurred on 25 April 2015, at a depth of ~15 km. The observed CIDs are identified to be related to gravity waves, acoustic waves, and seismic Rayleigh surface waves. Gravity waves-related CIDs were mainly observed to the south and north of the epicenter; acoustic waves-related CIDs were recorded for 1000 km in all directions from the epicenter; CIDs related to Rayleigh waves could be observed only to the east of the epicenter. This directivity of Rayleigh wave-related CIDs is strongly consistent with azimuthal characteristics of the ground vibrations.

Ding F et al. (2016) used the GPS network in northwest China and central Asia to monitor traveling ionospheric disturbances (TIDs), which were possibly excited by the large meteorite blast over Chelyabinsk, Russia, on 15 February 2013. Two TIDs were identified from GPS network observations. The first TID was observed 13 min after the blast, within a range of 270–600 km from the blast site. It propagated radially from the blast site with a mean velocity and period of 369 m/s and 12 min, respectively. The second TID was observed in northwest China, 2500–3100 km from the blast site, 1.5 h after the time of the blast. The latter TID propagated southeastward with a velocity and period of 410 m/s and 23 min, respectively. Severe dissipation of the perturbation TEC amplitude was observed. No TIDs propagating in a global range were found after the meteorite blast. Features of TIDs were compared with those excited by early nuclear explosion tests. It is inferred that the energy release of the Chelyabinsk meteorite blast may not have been large enough to excite such global range ionospheric disturbances as some early nuclear explosions did.

Yan XX et al. (2017) use data from the Crustal Movement Observation Network of China (CMONOC) and the IGS (International GNSS Service) to analyze statistically the behavior of the total electron content (TEC) perturbation before 30 M_w 6.0$^+$ earthquakes from 2000 to 2010 in China. TEC anomalies are detected before 20 of these earthquakes. The anomalies occur mostly within 2–6 days before the shocks, significantly during the afternoon period, 12: 00-20: 00 LT. The work illustrates the difficulties of searching for precursors of earthquake in the ionosphere, but also calls attention to the potential importance of effects of atmospheric waves on the ionosphere, as well as of the applicability of statistical approaches.

Liu J et al. (2016c) studied synchronous seismo-ionospheric disturbances associated with the Sumatra Indonesia M_s 7.2 earthquake that occurred on 5 July 2005. Ionospheric plasma disturbances in GPS-TEC and increases in N_e at 710 km were found on 4 July, before the earthquake; plasma densities at three different altitudes increased on 7 July, after the earthquake. It is interesting that all the disturbances were not just above the epicenter. TEC perturbations occurred to the east of the epicenter for the two days, and electron density enhancement at 710 km moved to the west of the TEC perturbations on 4 July.

Chen G et al. (2016c) analyze data from three digisondes and one Doppler receiver located in East Asia to investigate the far-field ionospheric response to westward-propagating gravity waves generated by the 2011 Tohoku tsunamigenic earthquake. Oscillations in the ionosphere of periods between 20 and 36 minutes were identified as having been induced by the tsunami that followed the earthquake. The use of multisite remote sensing for examining tsunami-induced waves in the ionosphere may open new perspectives in oceanic monitoring and future tsunami warning systems.

Ionospheric observations nets were established recently in order to monitor seismo-ionospheric phenomena. One is the vertical ionosonde net in southwestern China (Liu J et al., 2016a). Using these data, some perturbations were found before the Nepal M_s 8.1 earthquake on 25th April 2015. Another is the China Seismo-ionospheric Ground-based Monitoring Network (CSGMN) in Northern China (Liu J et al., 2016b). It was found that oblique sounding data present similar change characteristics to those seen in vertical sounding data. Zhou C et al. (2017a) developed an electric field penetration model for seismo-ionospheric research. Based on the three dimensional ionospheric electric field model, both the horizontal and vertical components of abnormal electric field exist at ionospheric heights due to the Lithosphere-Atmosphere-Ionosphere Coupling (LAIC) electric field penetration.

Shen XH and Zhang XM (2017) investigated the spatial distribution of hydrogen ions with the data from the DEMETER and DMSP satellites. At the 840 km altitude of the DMSP satellite, the seasonal variations of H^+ density are basically symmetric at the two winter hemispheres; but at the 660 km altitude of DEMETER, the peak H^+ is enhanced in the northern hemisphere in the December season and quite weak at both hemispheres in June. Changes in the observed distribution of H atoms and neutral wind in the upper atmosphere suggest, that the upwelling movement at the equatorial area and the northward neutral wind may play important roles in H^+ peak drift in the December season at DEMETER satellite altitude when it is below the transition height and H^+ is not the main composition.

Shen XH et al. (2017) conducted a comparative study on propagation of VLF radio signals before strong earthquakes, based on ground-based and space-based observations. The ground observations of VLF radio signals show that the disturbance intensity of VLF waves' amplitudes relative to the background gets an enhancement, one day before the 2010 M_s 7.1 Yushu earthquake, of more than 22% at 11.9 kHz, 27% at 12.6 kHz, and 62% at 14.9 kHz along the path from Novosibirsk-TH. Ground and space based observations of VLF radio wave propagation before the 2010 Yushu earthquake provides convincing evidence of the existence of seismic anomalies. There is a decrease of the signal to noise ratio (SNR) in the power spectral density data of 14.9 kHz VLF radio signals four days before the Yushu earthquake.

3. Ionospheric Climatology and Modelling

Chen YD et al. (2016a) investigated the latitudinal structure of topside ion density (N_i) using ROCSAT-1 and DMSP N_i observations.

The double-peak structure of EIA may exist at 600 km but is not a prevalent characteristic at 840 km, even at solar maximum sunset hours. The double-peak EIA structure begins to appear at noontime (Figure 8), being later than the appearance of the EIA in F_2 peak region. The pronounced EIA induced by the strong prereversal enhancement at solar maximum begins to appear at 19: 00 LT and can last to premidnight. EIA structure shows evident longitudinal difference. Pronounced EIA exists in the vicinity of 100°E at 13: 00 LT at the two equinoxes and the June solstice; at the December solstice it appears at more extensive longitudes (about 90°E to 240°E).

Chen YD et al. (2016b) used radio occultation observations of the Constellation Observing System for Meteorology, Ionosphere, and Climate (COSMIC) to study the dusk-to-nighttime enhancement (DNE) of summer N_mF_2 (Figure 9). They presented the global distributions of the magnitude and the peak time of the DNE at solar minimum as well as the role of the DNE in the N_mF_2 diurnal cycle. The DNE mainly exists in three regions (one in the Southern Hemisphere and two in the Northern Hemisphere). Their distribution is related to geomagnetic configuration. The DNEs are much more prominent in the southern than in the northern summer hemisphere. The positive geomagnetic declinations and the smaller geomagnetic inclinations at higher geographic latitudes over the South Pacific are crucial for the prominent DNEs in the southern summer hemisphere; they result in larger upward plasma drift at higher latitudes where photoionization is still significant during sunset and evening hours.

Chen YD et al. (2017) investigated the interhemispheric asymmetry of the topside ionosphere using total ion density (N_i) measurements from the ROCSAT-1 mission. The N_i asymmetry during the local time sector of late afternoon to midnight around the March equinox of 2000, a solar maximum year, was analyzed for two longitude sectors with larger geomagnetic declinations (positive at 120°W–180°W and negative at 0–60°W). The asymmetry of EIA crests is consistent with (but much weaker than) that of N_i at middle dip latitudes in each longitude sector, and the asymmetry is contrary between the two longitude sectors. The zonal wind induces opposite vertical plasma transports between the two hemispheres under the effect of geomagnetic declination. For the asymmetry of EIA crests, the effect of vertical plasma transport dominates over that of trans-equatorial plasma transport. Zonal wind reversal around sunset causes N_i at middle dip latitudes to increase in one hemisphere while quickly decreasing in the other; this phenomenon induces a quick reversal of asymmetry at about 18: 00 LT (Figure 10). Ion composition at 600 km was found to have asymmetries similar to those of N_i, indicating that wind-induced vertical plasma transport is important for topside ion composition.

The EIA and ionospheric annual asymmetry are two interesting ionospheric structures. Based on the TIEGCM simulations, Dang T

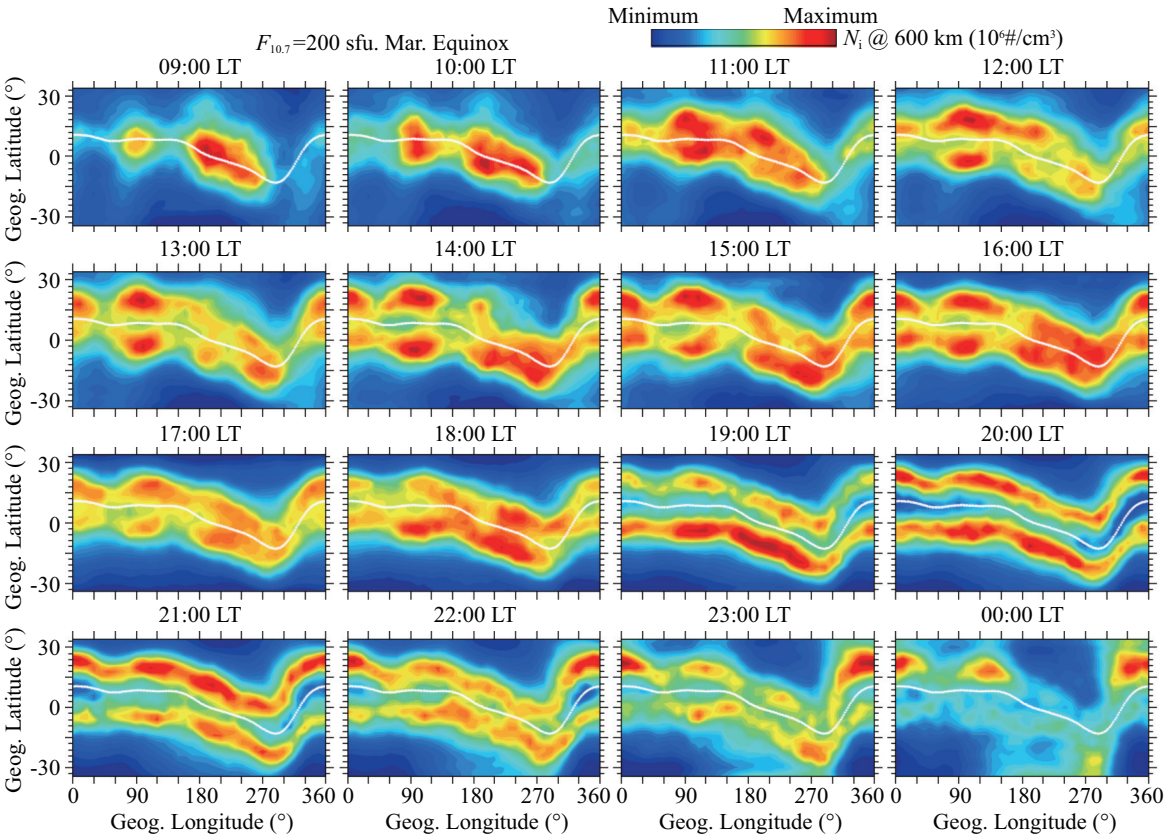

Figure 8. Local time evolution at the March equinox of the longitude-latitude map of 600 km N_i at the high solar activity level of $F_{10.7}$= 200. The color bar scales at different local times are not uniform in order to highlight the characteristics of the longitudinal and latitudinal variations of N_i at each local time. The white lines in each plot denote the dip equator. After Chen YD et al. (2016a).

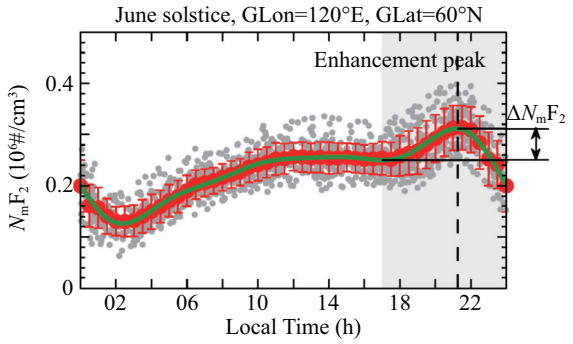

Figure 9. Local time variation of COSMIC N_mF_2 within the bin centered at (120°E, 60°N) at June solstice. Scatter plots are COSMIC measurements; red dots and error bars are the averages and associated standard deviations of the N_mF_2 data within 2-hour moving windows, respectively; the solid line is the fourth-order Fourier fitting of the running averaged N_mF_2. The vertical dashed line denotes the peak of N_mF_2 DNE; ΔN_mF_2 is the magnitude of N_mF_2 DNE. After Chen YD et al. (2016b).

et al. (2016) investigated the physical mechanism of EIA's hemispheric asymmetry. Their results illustrated that the neutral wind variations dominate the EIA hemispheric asymmetry and its longitudinal variations. For the ionospheric annual asymmetry, based on the simulations of the Global Mean Model, Lei JH et al. (2016a) showed that the O_2 dissociation process associated with the solar EUV flux changes between December and June cannot provide a significant increase in the ionospheric annual asymmetry. Dang T et al. (2017) further indicated, utilizing TIEGCM simulations, that the Sun-Earth distance effect on the photochemical processes is the major contributor. Moreover, using COSMIC radio occultation measurements, Luan XL et al. (2016) first reported the daytime double crests structure of h_mF_2. The double crests are evident at the March equinox, become less obvious during the September equinox, and disappear at the solstices.

Yu SM et al. (2016b) used TEC observations at two stations (CHAN (43.8°N, 125.3°E) and URUM (43.7°N, 87.6°E)) to study morphological features of longitudinal differences of ionospheric electron density. Although the zonal wind does play an important role on average, it is not sufficient to explain all the observed features; the longitude dependence of the meridian wind must be considered. Comparative studies between the Asian and American sectors are expected to yield more insights into the neutral and meteorological factors on the ionosphere.

Le HJ et al. (2016b) developed a two-dimensional ionospheric model that assimilates the observations of N_mF_2 and h_mF_2 derived from five ionosonde stations along the 120°E meridian, using three-dimensional variation techniques (3DVAR) based on a physics-based ionosphere theoretical model. Using data of N_mF_2 and h_mF_2 from five ionosonde stations located from northern to southern China, their system can produce well-assimilated results along the 120°E meridian plane.

Data assimilation is one of the important GNSS applications in recent years and relies on a tremendous amount of data processing and computation. She CL et al. (2017) assimilated the worldwide multisource TEC observations during the magnetically quiet time into a parameterized four-dimensional model, which is developed from the IRI-2012 model by spherical harmonic (SH) expansions in the horizontal and empirical orthogonal functions (EOFs) in the vertical. The multisource TEC data included the TEC from ground-based GPS, LEO radio occultation (RO), and the oceanic altimeter. She CL et al. (2017) reanalyzed the TEC, f_oF_2, and N_mF_2 and compared those data to the CODE global TEC, the ionosonde f_oF_2 at middle-latitudes, and the retrieved N_mF_2 from COSMIC RO observations, respectively. As shown in Figure 11, the reanalyzed and the International Reference Ionosphere (IRI) results were consistent with the observations. The reanalyzed results perform better than the IRI model. The assimilating of multisource TEC data into parameterized models can reanalyze the global TEC and electron density and improve the performance of

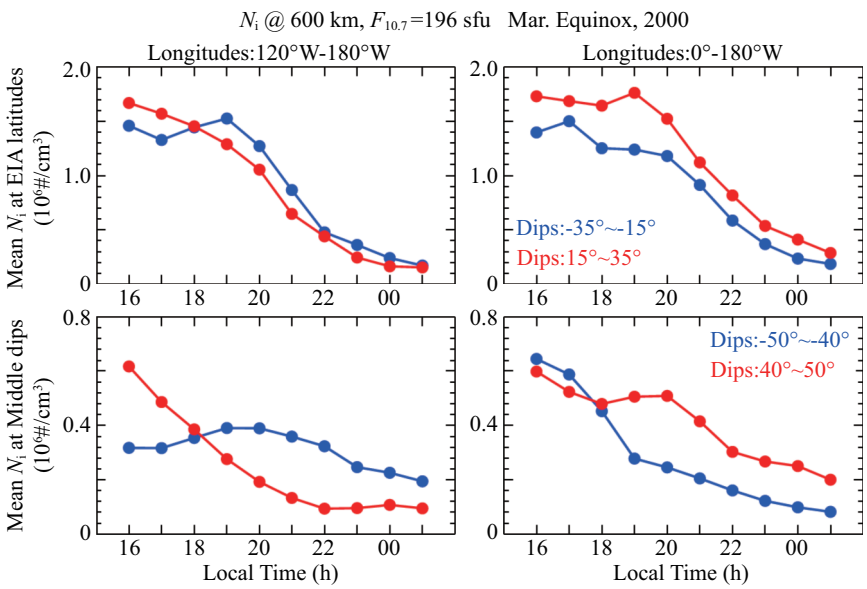

Figure 10. Local time variations of ROCSAT-1 N_i around the March equinox, 2000. After Chen YD et al. (2017).

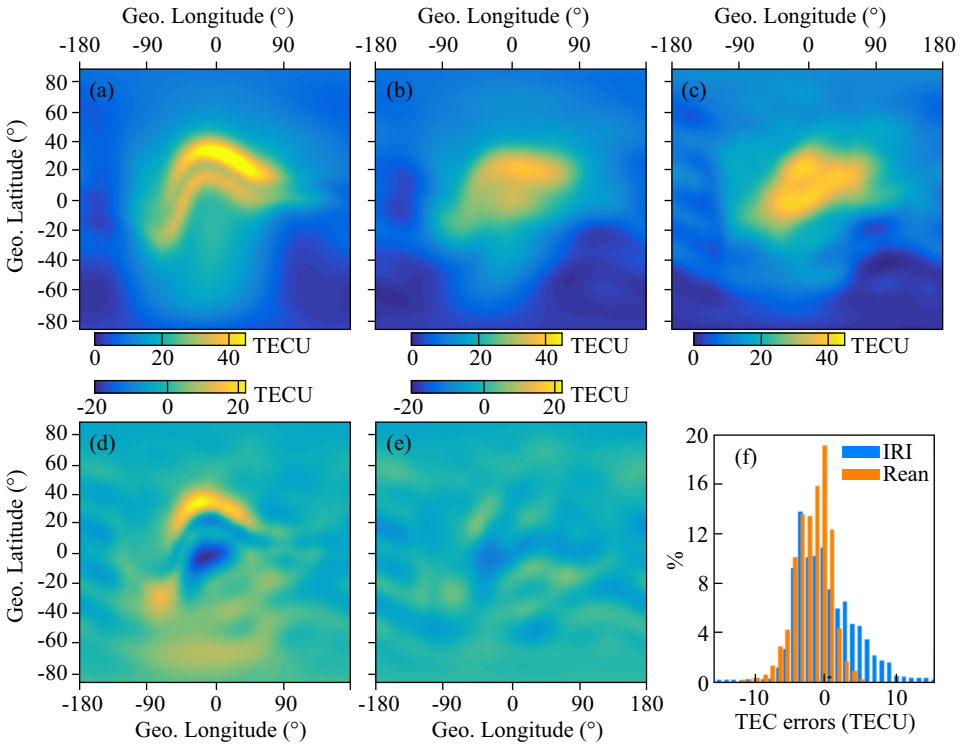

Figure 11. Global TEC maps from (a) IRI model, (b) reanalysis and (c) CODE; (d) GIM TEC errors of IRI against CODE, and (e) reanalysis results against CODE; (f) the histogram of GIM TEC errors at 14: 00 UT in August, 2011. After She CL et al. (2017).

IRI model.

The midlatitude ionospheric trough is one of the important features of the ionosphere. Empirical orthogonal function analysis was used to construct an empirical model of the TEC in the middle to high latitudes. The analysis of Le HJ et al. (2017) provides unprecedented detail of the local time, seasonal, solar activity, and geomagnetic activity variations of the total electron content in the latitude range of 40°N–75°N, focusing on the variation of midlatitude trough. The results show that the trough minimum position has significant local time, seasonal, and geomagnetic activity dependences but slight solar activity dependence.

The EST (ionospheric equivalent slab thickness) is a measure of the thickness of the ionospheric profile, defined as the ratio of TEC to N_mF_2. Huang H et al. (2016) retrieved EST from TEC data obtained from Global Ionospheric Map (GIM) and N_mF_2 retrieved from the ionospheric radio occultation data from COSMIC. Theirs is the first analysis to show spatial and temporal features of the global ionospheric slab thickness. Enhancements in EST are found in presunrise and postsunset hours. Moreover, higher slab thickness exists to the east of WSA. This feature is supposed to be related to the effects of geomagnetic declination-related plasma vertical drifts.

Yang CJ et al. (2017) combined topside *in situ* ion density data from the Communication/Navigation Outage Forecast System (C/NOFS) and the electron density profiles from COSMIC RO measurements to study spatial and temporal variations of the ionospheric upper transition height and the oxygen ion density scale height.

The reliability of the model in reproducing the topside ionosphere and plasmasphere is a challenging task. Zhang ML et al. (2017) compared the topside ionospheric and plasmaspheric electron contents (TPEC) in the altitude range of ~800 to 20200 km with the IRI_Plas model results for the low (2008) and high (2012) solar activity years. The TEC data (podTEC) are derived from the upward-looking precise orbit determination antenna on board COSMIC low Earth orbit (LEO) satellites tracking the GPS signals. The comparison shows that the IRI_Plas model is able to reproduce reasonably well the main features of the observational TPEC's latitudinal, diurnal, and seasonal variation tendency when no longitudinal difference is taken into account. The IRI_Plas model tends to reproduce a double-peak structure in the low-latitude region, which is not present in the observational results.

The upward looking ionospheric TEC from the MetOp-A and TSX satellites during 2008–2015 has been used by Zhong JH et al. (2017) to study the longitudinal variations of the topside ionosphere and plasmasphere. Significant longitudinal variations are present in the topside ionosphere and plasmasphere at low latitudes, which are different from the corresponding longitudinal variations of electron densities around the F_2 peak and orbital altitudes. The difference indicates that the topside ionosphere structure is strongly influenced by physical processes in the topside region, rather than being a pure reflection of the ionospheric F_2 peak structure.

Yu T et al. (2017) presented a method for estimating daily averaged peak height of the OH airglow layer from a ground-based meteor radar (MR) and a Fabry-Perot interferometer (FPI). They compared simultaneous 4-year measurements of winds by a MR

and a FPI at two adjacent stations over center China and from the Thermosphere Ionosphere Mesosphere Energetics and Dynamics/Sounding of the Atmosphere using Broadband Emission Radiometry (SABER) instrument. Some similarities are found between the SABER OH 1.6 μm observations and airglow peak heights. The OH airglow peak heights are found generally to peak at an altitude of 87 km, varying frequently between 80 km and 90 km.

The latest version IRI2016 provides three options for the F_2 peak height h_mF_2: AMTB2013, SHU-2015, and BSE-1979. Zhao XK et al. (2017) used ionosonde h_mF_2 data at Mohe, Beijing, Wuhan, and Sanya, ranging from year 2007 to 2016, to assess the performance of these three options of IRI2016. As shown in Figure 12, the variability of the observed h_mF_2 versus local time, seasons, and levels of solar activity could be reproduced well by all three options. However, the SHU-2015 option performs best at these four stations, followed by BSE-1979; the AMTB2013 option is worst. Generally, the AMTB2013 and BSE-1979 options overestimate the h_mF_2 values, while the SHU-2015 option mainly underestimates the h_mF_2 values. Overall, the authors recommend the SHU-2015 h_mF_2 option when using the IRI2016 model to calculate h_mF_2 over the Chinese region.

Zhou S et al. (2016) used auroral energy flux data observed by TIMED/GUVI and DMSP/SSUSI to investigate the nightside auroral distribution. They found that the nightside auroral power was reduced by ~42% at solar maximum ($F_{10.7}$=200) compared to solar minimum ($F_{10.7}$=70) for *Kp*=1. This decreasing tendency became less as the *Kp* index increased. These phenomena might be caused by the increasing background ionospheric ionization as the *Kp* index rises, which could limit the plasma gradient, leading to a weak dependence of the nightside aurora on solar activity when *Kp* increased.

Using 2 years of magnetic field measurements from the Swarm constellation, Zhou YL et al. (2016a) represented the tidal characteristics derived from the longitudinal gradient of EEJ when the longitudinal wave number 4 (WN4) pattern is known to be most prominent. The EEJ intensity is derived from the average of the Swarm A and C current estimates. The EEJ peaks around 11: 30 LT and exhibits a clear WN4 pattern. These features are compatible with earlier CHAMP observations.

Further, Zhou YL et al. (2016b) used more than a decade's *in situ* electron density observations from CHAMP and GRACE satellites to investigate the solar activity dependence of nonmigrating tides at both low and middle latitudes. The longitudinal patterns of F region electron density are found to vary with season and latitude. There is a WN4 pattern around September equinox at low latitudes and WN1/WN2 patterns during local summer at the southern/northern middle latitudes.

Using data collected from the Arecibo incoherent scatter radar during January 14–21, 2010, Gong Y et al. (2016b) conducted an analysis of the thermospheric midnight temperature maximum (MTM), a large increment of temperature around midnight. They found that the variation of meridional wind and the MTM are consistent with the WAM model studies, which suggests that the variation is due to effects from an upward propagating terdiurnal tide. Their results provide direct observational evidence of the important role that propagating upward terdiurnal tides play in causing the MTM, which supports the WAM simulations.

Ma Z et al. (2017) presented an analysis of the responses of quasi-2-day waves (QTDW) to the 2013 sudden stratosphere warming

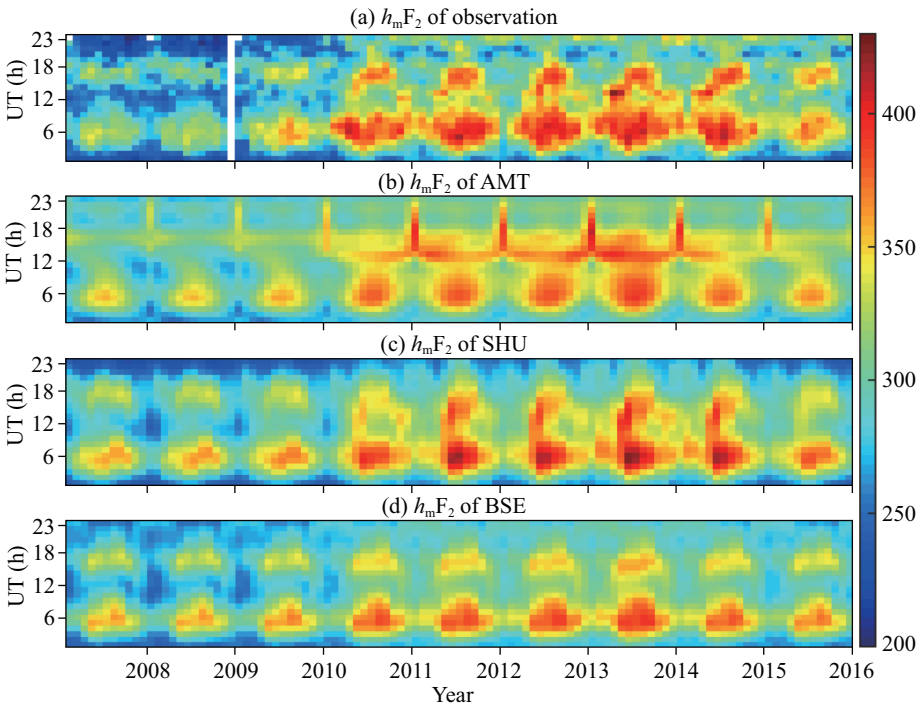

Figure 12. Variations of the monthly median h_mF_2: (a) ionosonde observation data, (b) AMT, (c) SHU and (d) BSE at Sanya station. After Zhao XK et al. (2017).

(SSW) in the mesosphere and lower thermosphere (MLT) region. Their study is based on data recorded by a meteor radar chain along the 120°E meridian in the Northern Hemisphere. It is the first time that an enhancement of the QTDW in the neutral wind during the 2013 SSW is observed at mid-latitudes in the Northern Hemisphere. The consistent variations of the QTDWs and the mean neutral wind at the four stations are very likely associated with the SSW.

Jiang CH et al. (2016b) studied the latitudinal variation of the peak time of postmidnight enhancements in F layer electron density based on observations from low latitude ionosondes. The enhancement peaks earlier at lower geomagnetic latitudes for the northern hemisphere. They proposed that the combined effect of the geomagnetic inclination and transequatorial meridional wind might be the main driving force for latitudinal variation of the local time of the occurrence.

4. Ionospheric Irregularity and Scintillation

In order to better understand the day-to-day variability in the occurrence of equatorial plasma bubble (EPB) producing ionospheric scintillation and its predictability, Li GZ et al. (2016) performed a cooperative campaign, with radar multibeam steering measurements simultaneously conducted at Kototabang (0.2°S, 100.3°E, dip latitude 10.4°S) and Sanya (18.4°N, 109.6°E, dip latitude 12.8°N), to investigate the generation of EPB and its relationship to the atmospheric Intertropical Convergence Zone (ITCZ) in Southeast Asia. As shown in Figure 13, the two selected stations are separated only by 9.3° in longitude, with almost the same magnetic declination and offset of the magnetic equator from the geographic equator, so that one of the important factors affecting the generation of EPB, the evening pre-reversal enhancement

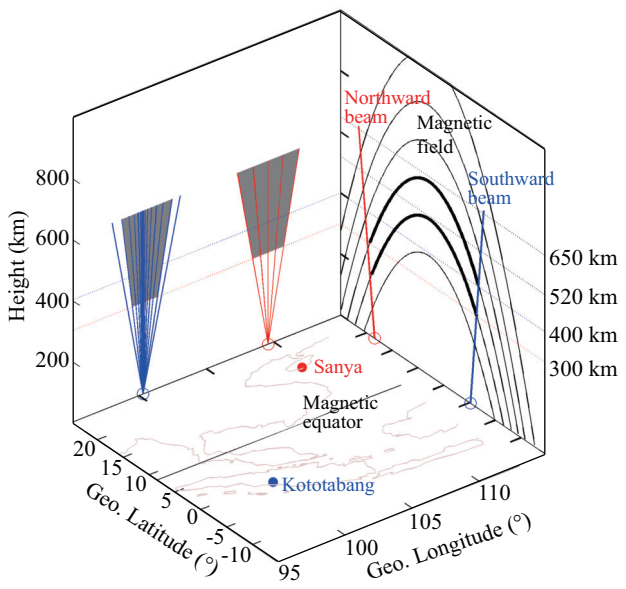

Figure 13. A schematic diagram showing geographic latitude-longitude locations and beam directions of Kototabang and Sanya radars. The radar-scanned area with shading shows the longitudes where bubbles were classified into two groups, generated locally and drifted from elsewhere. After Li GZ et al. (2016).

of the eastward electric field (PRE), does not change much between the two longitudes. The results showed for the first time that there is an extremely large difference in EPB generation but not in EPB occurrence. The EPB occurrence rates are comparable, but the total number of nights with locally generated bubble (i.e., generation rate) over Kototabang is clearly more than that over Sanya. Further analysis reveals that a more active ITCZ is situated around the longitude of Kototabang. The authors propose that the enhanced ionospheric bubble generation at Kototabang's longitude could be caused by a higher gravity wave activity associated with the more active ITCZ, where the GWs could provide the seeding source for bubble development.

The bottom-type irregularity scattering layer (BSL) serves as a possible telltale of equatorial spread F (ESF). The BSL is generally observed in the ionospheric F region bottomside after sunset. Using simultaneous multibeam radar measurements at the two low-latitude stations, Sanya and Fuke (19.3°N, 109.1°E; dip latitude 14°N) in China, Li GZ et al. (2017) presented the first observation of F region bottomtype irregularity scattering layer (BSL) generated before sunset. Similar oscillations are found in BSL echo Doppler velocity and F layer height. The presunset BSL could be linked to the bottomside large-scale wave structure, implying an important role of gravity waves in the generation of the presunset F region bottom-type irregularities.

Hainan coherent scatter phased array radar (HCOPAR) located at low latitude of China has recorded extremely rare daytime F region irregularities, at noon of 22 July 2013 and 23 May 2016 (Figure 14). The two field-aligned irregularities (FAIs) appeared in the topside F_2 layer and presented small Doppler velocities and narrow spectral widths. The fan sector maps show that the FAIs moved northward with almost no zonal speed. The midday FAIs over Hainan may drift along the magnetic field lines from higher altitudes in the south and are most likely the remnant of previous night's bubbles (Chen G et al., 2017a).

The association between the sporadic E (Es) layer and the metallic layer is a historic topic. Xue XH et al. (2017) reported an overturning-like structure of the thermospheric sodium layer (TSL) in the altitude region of ~100–120 km, observed by a sodium lidar at Haikou (20.0°N), China, on July 29, 2012. The overturning-like sodium layer was first seen as an upwelling from the top of the sodium layer (~102 km) to an altitude of ~118 km from 14: 55 to 15: 50 UT that then descended gradually from its apex with a speed of 3.5 km/h. Observations from the COSMIC radio occultation (RO) and three ionosondes exhibited abrupt perturbations in the radio occultation SNR profiles and spread Es in the ionograms, respectively, indicating the existence of complex Es around Haikou. Moreover, VHF radars located at Sanya (18.4°N, 220 km away from Haikou) and Fuke (19.5°N, 130 km away from Haikou) both recorded strong E region field-aligned irregularity (FAI) echoes from an altitude-extended structure covering altitudes of 100–140 km, which correlates well with the overturning-like structure of the thermospheric sodium layer (Figure 15). The good agreement between occurrence time of the sodium layer (and FAI) structure and of complex Es could indicate a close correlation between them. The authors suggest that the chemical reaction in the course of the complex Es (with altitude-deformed structure) could

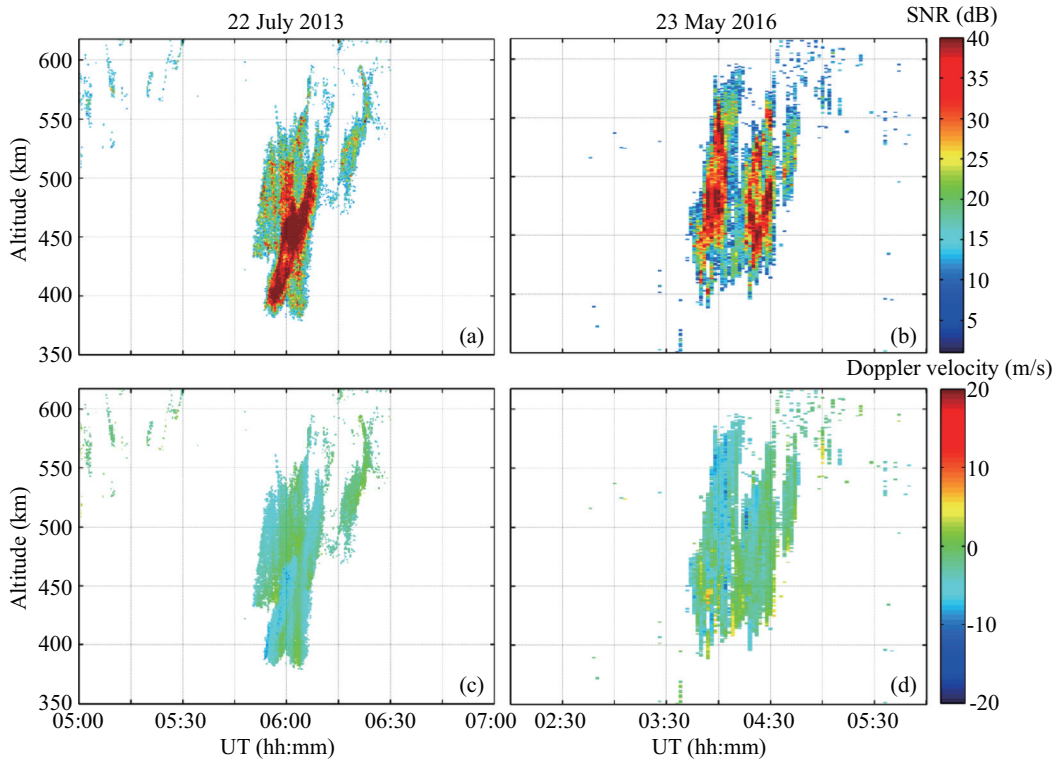

Figure 14. Daytime F-region irregularities recorded on (left) 22 July 2013 and (right) 23 May 2016. The altitude-time-intensity plots and the corresponding Doppler velocity plots are placed in the top and bottom rows, respectively. LT = UT+7.3 hr. After Chen G et al. (2017a).

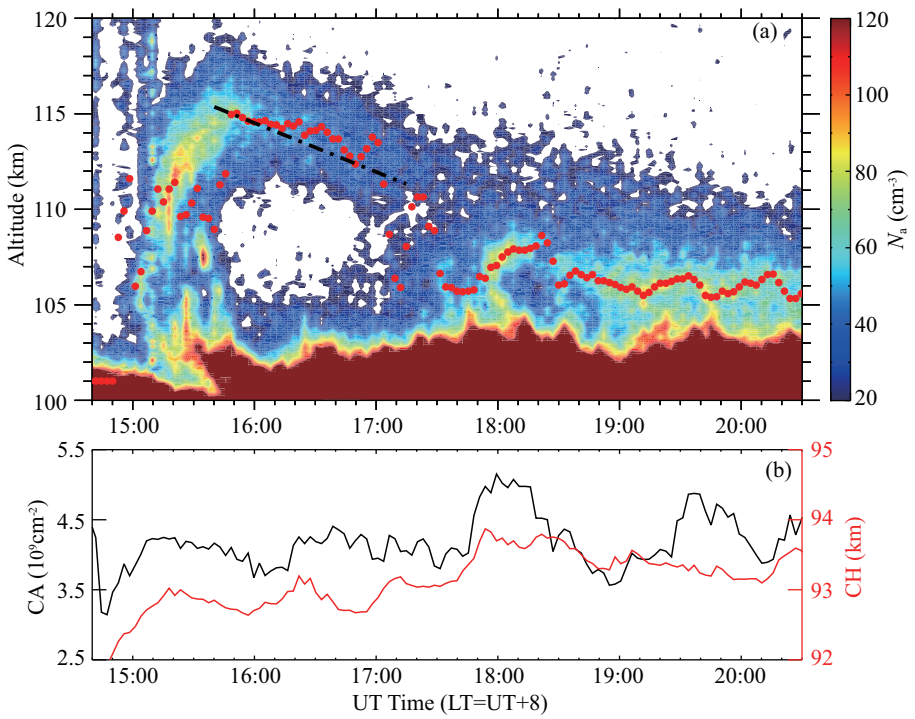

Figure 15. (a) The contour plot of the upper sodium number density within 100–20 km during 14: 40–20: 30 UT on July 29, 2012, observed by sodium lidar. The red dots show the weighted centroid height of sodium between 105 and 125 km, and the dash-dot line shows the linear fit of the weighted centroid height during 15: 40–17: 20 UT. (b) The abundance density (black) and the centroid height (red) of the whole sodium layer. After Xue XH et al. (2017).

produce sufficient sodium atoms to cause the formation of the observed upwelling of the sodium layer. Correspondingly, FAI altitude-extended structure could be generated through the gradient drift instability in the altitude-extend (deformed) Es, which

provide plasma density gradients to support the instability development.

The Beidou geostationary orbit (GEO) satellites could provide fidelity TEC observations to study ionospheric variability. Huang FQ et al. (2017) used TEC data from a Beidou GEO receiver network to observe and investigate ionospheric longitudinal variations within the zonal scale of 1000 km over Central China. They found that pronounced daytime longitudinal gradients within the distance of 1000 km are present in BeiDou GEO TEC; the maximum TEC longitudinal gradient can reach 45 TECU.

Based on ionospheric TEC derived from 250 GNSS receivers over China, Xiong B et al. (2016) studied diurnal variation and day-to-day variability of the ionosphere. Measurements from the GEO satellites of the BeiDou Navigation Satellite System (BDS) clearly demonstrate ionospheric day-to-day variability and east–west differences (Figure 16), even in a region with quite small longitude differences (3.52°–11.31°). The east-west differences in TEC are obvious at 11:30 local time on 23 January 2015 with a maximum in TEC about 7 TECU in longitude difference of 11.31°. The east-west differences in TEC may be associated with the east-west gradient of geomagnetic declination. Regional ionospheric maps are constructed.

Convective activity in the lower atmosphere has significant influence on the upper atmosphere. Yu BX et al. (2015) used a superposed epoch analysis (SEA) to analyze the relationship between the ionospheric sporadic E (Es) layer and atmospheric lightning events. The magnitude of lightning-associated enhancement of the Es layer is likely associated with lightning stroke energy.

Zuo X et al. (2016) presented the first study based on scintillation observations from the Chinese FY-2 geostationary meteorological satellite (86.5°E) observed at Guangzhou (23.2°N, 113.3°E, dip 18°N) and simultaneous VHF (47.5 MHz) coherent radar measurements from Sanya (18.3°N, 109.6°E, dip 13°N) during equinoctial months of 2011 and 2012. The authors describe the relationship between L-band scintillation patches on the propagation path of FY-2 satellite and extended 3-m irregularity structures over South China (Figure 17). There is nearly a one-to-one correspondence between the plumes and the scintillation patches. The zonal drift velocity of the irregularities was estimated by comparing the onset times of the scintillation and plume. The irregularities were found to drift eastward at speeds ranging from tens of meters to one hundred meters per second.

A statistical analysis of sporadic E layer occurrences was conducted by Zhou C et al. (2017b). They collected 5-year ionosonde data from four stations in the midlatitude China region. The occurrence of the sporadic E layer strongly depends on local time and season. The atmospheric tidal waves and planetary waves might play an important role in generation of mid-latitude sporadic E layer. Moreover, the sporadic E layer also tends to increase with the level of geomagnetic activity.

Zhang QH et al. (2016a) reported simultaneous global monitoring of a patch of ionization and *in situ* observations of ion upflow at the center of the polar cap region during a geomagnetic storm. These observations indicate strong fluxes of upwelling O^+ ions originating from frictional heating produced by rapid antisunward flows of the plasma patch. Statistical results from crossings of the central polar cap region by Defense Meteorological Satellite Program F16–F18 from 2010 to 2013 confirm that the field-aligned flow can turn upward when rapid antisunward flows appear, with

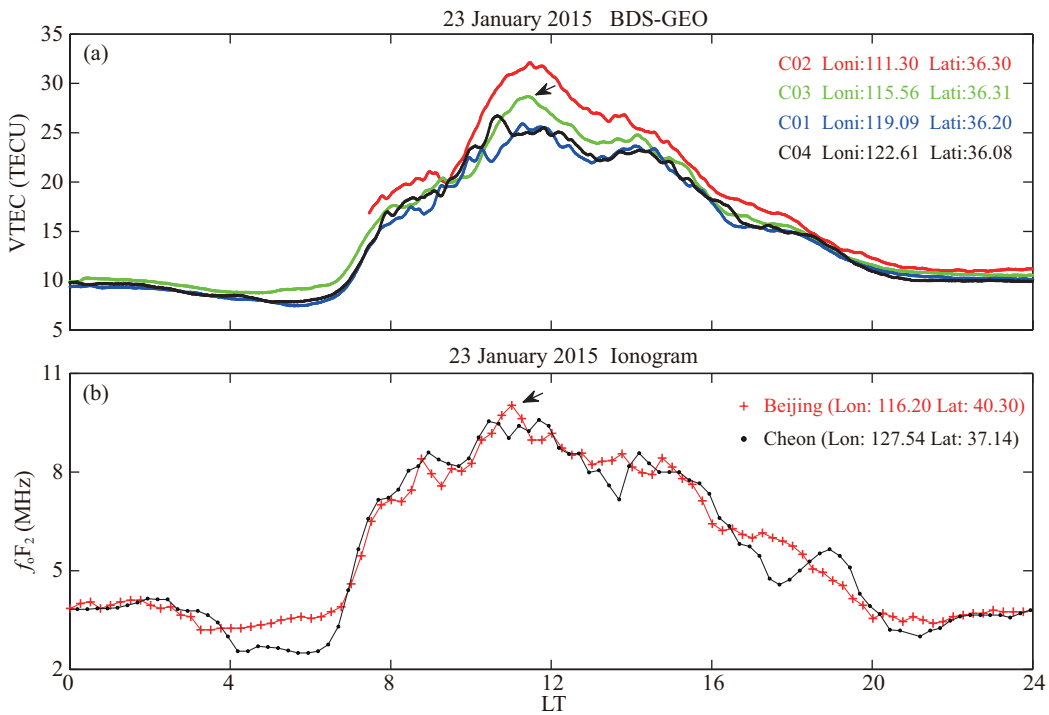

Figure 16. (a) Temporal variations of the vertical TEC derived from BeiDou GEO satellites (Satellite No. C01-C04) at Beijing on 23 January 2015. (b) Temporal evolution of f_0F_2 observed at Beijing and Cheon on 23 January 2015. After Xiong B et al. (2016).

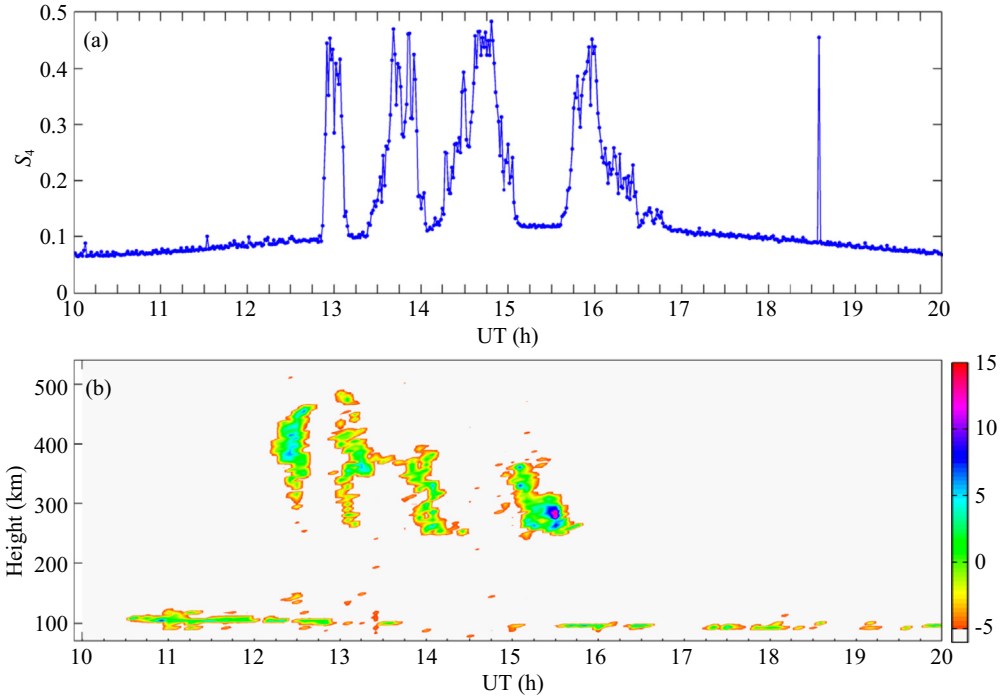

Figure 17. The temporal variation of S_4 values on the link of FY-2 satellite for the postsunset to post midnight interval (LT=UT+8h) on October 24, 2011 (a) and simultaneous Range-time-intensity (RTI) map of backscatter echoes obtained from the Sanya VHF radar (b). After Zuo X et al. (2016).

consequent significant frictional heating of the ions, which overcomes the gravity effect. The authors suggest that such rapidly moving patches can provide an important source of upwelling ions in a region where downward flows are usually expected. These observations give new insight into the processes of ionosphere-magnetosphere coupling.

Zhang QH et al. (2016b) reported continuous monitoring of a polar cap patch, encompassing its creation and evolution (Figure 18) that differs from classic behavior. The patch was formed from the storm enhanced density plume, by segmentation associated with a subauroral polarization stream generated by a substorm. Its initial antisunward motion was halted due to a rapid change in interplanetary magnetic field (IMF) conditions (from strong southward to strong eastward with weaker northward components), and the patch subsequently evolved very slowly behind the duskside of a lobe reverse convection cell in afternoon sectors, associated with high-latitude lobe reconnection, much of it fading rapidly due to an enhancement of the ionization recombination rate. This differs from the classic scenario, in which polar cap patches are transported across the polar cap along the streamlines of twin-cell convection patterns, from day to night. This observation provides important new insights into patch formation and control by the IMF, which must be taken into account in F region transport models and space weather forecasts.

Using two B-spline basis functions of degree 4 and ionospheric scintillation data from a Global Positioning Satellite System (GPS) scintillation receiver at the South Pole, Priyadarshi et al. (2016) reproduced ionospheric scintillation indices for the periods of the six X-class solar flares in 2013. These reproduced indices filled the data gaps, and are serving as a smooth replica of the real observations. In either event, these modeled scintillation indices are minimizing the geometrical effects between GPS satellite and the receiver. Six X-class solar flares have been studied during the summer and winter months, using the produced scintillation indices based on observations from the GPS receiver at South Pole and the *in situ* plasma measurement from the associated passing of Defense Meteorological Satellite Program devices. These results show that the solar flare peak suppresses the scintillation level and builds time-independent scintillation patterns; however, a certain time after the solar flare peak, complicated scintillation patterns develop at the high-latitude ionosphere and spread toward the polar cap boundary region. Moderate proton fluxes are substantially consistent with scintillation enhancements.

Wang Y et al. (2016) made a comparison between large-scale ionospheric irregularities and scintillations during a geomagnetic storm. Irregularities, such as storm enhanced density, middle-latitude trough, and polar cap patches, are clearly identified from the TEC maps. Clear scintillations appear at the edges of these irregularities. Phase scintillations (σ_φ) are larger than the amplitude scintillations (S_4) at the edges of these irregularities, associated with bursty flows or flow reversals with large density gradients. An unexpected scintillation feature appeared inside the modeled auroral oval, where S_4 were much larger than σ_φ most likely caused by particle precipitations around the exiting polar cap patches.

Based on *in situ* and ground-based observations, Zhang QH et al. (2017) identified a new type of "polar cap hot patch", of the same order of density enhancement as classical patches in the topside ionosphere. The classical polar cap patches are transported from

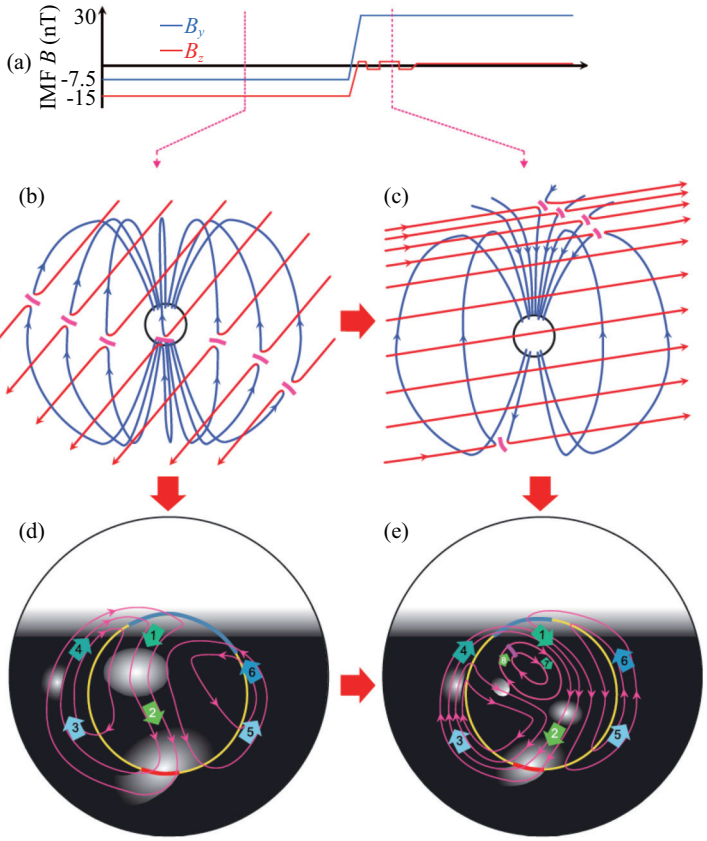

Figure 18. (a) Schematic of the response of the northern polar ionosphere to the IMF turning from strongly southward and weakly dawnward to strongly duskward, with a weak B_z varying around zero during a substorm recovery phase. Panels shown are (a) the IMF B_y and B_z components, (b and d) the morphology of dayside magnetic reconnection and the polar ionosphere for strong southward and weaker dawnward IMF, (c and e) the morphology of dayside magnetic reconnection and the polar ionosphere for strong duskward and weak northward IMF. After Zhang QH et al. (2016b).

the dayside sunlit region with dense and cold plasma, while the polar cap hot patches are associated with particle precipitations (therefore field-aligned currents), ion upflows, and flow shears. The hot patches may be produced by transported photoionization plasma into flow channels. Hot patches may lead to slightly stronger ionospheric scintillations of GNSS signals in the polar cap region than classical patches.

Zhima Z et al. (2017) presented a conjugate observation of whistler-mode electromagnetic hiss between the low earth orbit satellite DEMETER and the high-altitude elliptical orbit spacecraft THEMIS. Similar time-frequency structures are found in the ionospheric hiss (~350 to 800 Hz) captured by DEMETER and the plasmaspheric hiss (~350 to 900 Hz) recorded by THEMIS probes, including peak frequencies (~500 to 600 Hz), lower cutoff frequencies (~350 to 400 Hz) and upper cutoff frequencies (~730 to 800 Hz). The wave vector analyses show that the ionospheric hiss propagates obliquely downward to the Earth and slightly equatorward with right-handed polarization, suggesting that its source comes from higher altitudes. Ray tracing simulations with the constraint of observations verify that the connection of ionospheric and plasmaspheric hiss is physically possible through wave propagation. Zhima Z et al. (2017) suggest that the high altitude plasmaspheric hiss serves as one source of ionospheric hiss.

5. Global Navigation Satellite System (GNSS) Related Issues and Other Techniques

Global Navigation Satellite Systems (GNSS) now are widely used in ionospheric monitoring. The Chinese Beidou Navigation Satellite System (BDS) is operating with three kinds of constellations: medium Earth orbit, inclined geosynchronous satellite orbit, and geosynchronous Earth orbit. Hu LH et al. (2017) designed a compact, portable, and low-power GNSS observation instrument at the Institute of Geology and Geophysics, Chinese Academy of Sciences, named BG2 GNSS ionospheric monitor. It is capable of tracking BDS, GPS, and Global Navigation Satellite System (GLONASS) signals at sampling rates up to 5 Hz. The authors deployed the BG2 GNSS ionospheric monitors in China at 30 sites. The BDS GEO TEC data have unique value in some specific ionospheric studies because they are not influenced by the mixed effect of spatial and temporal ionospheric variability.

TEC is derived from the phase delay of GNSS signals and extensively used for studies on variations of plasma in both the ionospheric and plasmasphere. Using hundreds of ground-based GPS receivers, instantaneous TEC impulses were observed on 17 March 2015 when an interplanetary shock (IS) impacted on the Earth's magnetosphere. TEC impulses discriminate themselves from usual ionospheric disturbances and other dynamics in association

with the magnetic storm following the shock. It is suggested that the TEC variation is caused by shock-induced magnetospheric compression, which drives plasma to move earthward in the day side magnetosphere. Plasma moving from outside of GPS orbit (4.2 R_E) to inside contributes to the plasma content traversed by GPS ray path. The GPS TEC technique thus exhibits an unprecedented capability to sense plasma dynamics in the magnetosphere remotely (Hao YQ et al., 2017).

The uncertainty of differential code bias (DCB) is one of the main error sources in low Earth orbit (LEO) based TEC retrieval. To improve the accuracy and reliability of LEO-based TEC, Zhong JH et al. (2016a) propose an improved DCB estimation method (ZERO method) and optimize the parameter configuration in the least square method (LSQ method). They also illustrate that the long-term variation of LEO DCBs is partly associated with the GPS satellite replacement, and the periodic variation can be attributed to variation in the hardware thermal status. Li M et al. (2017a) conducted an analysis of the intra-day stability of the DCBs from the ground-based receiver. They found large fluctuations (as much as 9 ns or more between two consecutive hours) in the receiver DCBs. The impact on the extraction of ionospheric TEC of such significant short-term variations in receiver DCBs may be at a level of 12.96 TECu (TEC unit). The authors suggest that a preliminary analysis of characteristics of receiver DCB variations over short-term intervals should be made prior to estimation of daily multi-GNSS receiver DCB products.

Transient loss of lock (LOL) is one of the key space weather effects on the GNSS. However, lack of data have prevented investigation of the altitudinal features of GNSS LOL. The high vertical resolution of RO observations enables us to distinguish clearly, on a global scale, the signal cycle slip (CS) resulting from different ionospheric layers. Based on COSMIC RO observations during 2007–2011, as shown in Figure 19, Yue XA et al. (2016a) have comprehensively analyzed the CS occurrence and its correlation to the ionospheric weather phenomena such as Es, equatorial F region irregularity (EFI), and the ionospheric EIA. At low and equatorial latitudes, the CS in the E layer is dominated by the Es occurrence, while the CS in the F layer is mainly related to the EIA and EFI. In the polar region, the CS is primarily related to polar cap electron density gradients. The overall average occurrence of CS (>6 cycles) is ~23% per occultation, with the E (50–150 km) and F (150–600 km) layers contributing ~8.3% and ~14.7%, respectively.

Absolute TEC is converted under the widely used assumption of a Single-Layer Model (SLM). The conversion requires information on the Ionosphere Effective Height (IEH) and pierce points. Li M et al. (2017b) propose a new approach to determine the optimal IEH over China. In their method, the optimal IEH is selected as the one in which the difference between the converted VTEC using mapping function and the VTEC estimate interpolated by the combined IGS GIMs can be minimized. For single-frequency GNSS users over China, it would be better to place optimal IEH values in the range of 450–550 km, instead of 350–450 km, by taking into account their application demands, i.e., accuracy or integrity of navigation.

Zhang BC et al. (2017) develop a single-frequency approach that enables the joint estimation of vertical TEC and satellite differential code biases (SDCBs), using low-cost receivers. Numerical analyses clarify the performance of their approach by applying it to GPS L1 data collected by a single receiver under both quiet and disturbed ionospheric conditions. The accuracy of the estimated TEC ranges from a few tenths TECU to approximately 2 TECU. For most in view GPS satellites, daily estimates of absolute SDCBs have an error below 1 ns, compared with the values provided by the Centre for Orbit Determination in Europe.

During the years 2016 and 2017, some ionospheric and atmospheric detecting instruments were developed, including the MST radar, ionospheric oblique backscattering sounding system, and coherent scatter radar. The Wuhan mesosphere, stratosphere, and troposphere (MST) radar, part of the Chinese Meridian Project,

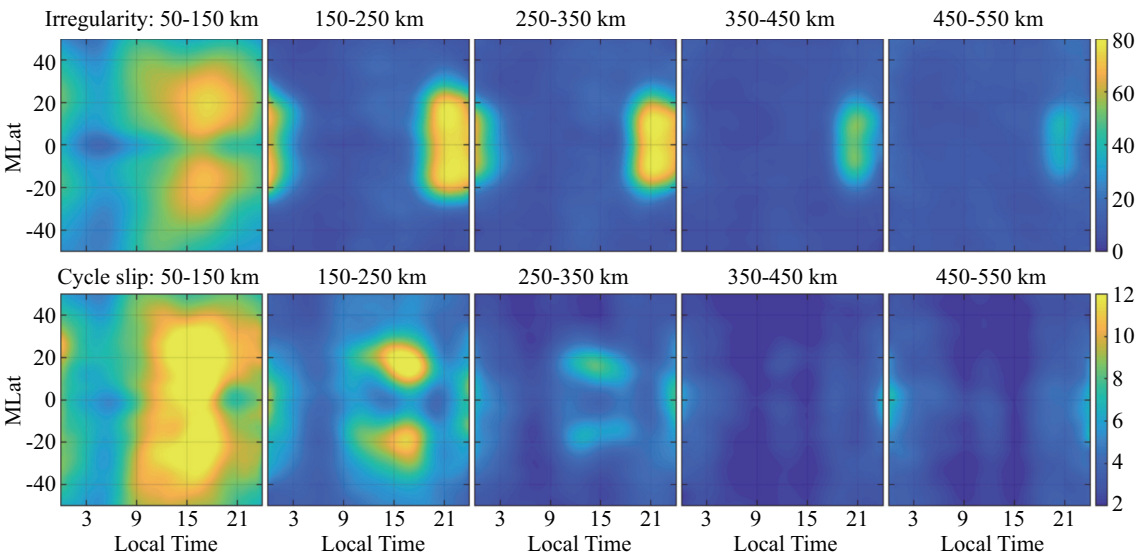

Figure 19. Top Row: MLT-MLat variation of ionospheric irregularity represented by S_4>0.3 (%); Bottom Row: the cycle slip occurrence rate per occultation (%) for different altitude intervals made by COSMIC during 2007–2011. After Yue XA et al. (2016a).

was designed and located in Chongyang of Hubei province, China, to investigate atmospheric dynamics from 3 to 100 km. The Wuhan MST is a monostatic radar operating at 53.8 MHz, with an active phased antenna array consisting of 576 three-element Yagi antennas arranged in a square grid of 96 m side length. The antenna array arrangement allows five symmetric radar beams of vertex, east, west, south, and north. The beamwidth is 3.2°, the maximum directive gain is 34.8 dB, and the total transmitting peak power is ~172 kW. The average power aperture product of the radars is 3.2×10^8 W·m^2. Thus, this pulse Doppler MST radar has the ability to study features of the midlatitude atmospheric turbulence and wind field vector from the troposphere to the lower thermosphere, with high spatiotemporal resolution. (Chen G et al., 2016b).

The Wuhan Ionospheric Oblique Backscattering Sounding System, with the addition of an antenna array (WIOBSS-AA), located in Chongyang, Hubei province of China, and became operational on 16 March 2015. The transmitting part of this radio system applies an array composed of five log-periodic antennas to form five beams that span an area to the northwest of the radar site. It is a kind of ionospheric backscatter sounding radar, and can detect ionospheric electron density information over a wide area (Cui X et al., 2016).

The Hainan coherent scatter phased array radar (HCOPAR) is one of the most important radio systems of the Chinese Meridian Space Weather Monitoring Project (Meridian Project) (Chen G et al., 2017b). The radar is located at Fuke station (19.5°N, 109.1°E, dip latitude 8.1°N), Hainan island, China, in order to observe the field-aligned irregularities in ionospheric E- and F-regions. It is operated with a peak power of 54 kW and uses Barker codes for good sensitivity. Its antenna array is composed of 18×4 five-element Yagi antennas. This antenna arrangement forms seven radar beams from −22.5° to 22.5° in azimuth with an angle step of 7.5°. The central beam points to due geographic north. Moreover, Qiao L et al. (2017b) designed a distributed ionospheric coherent scatter radar that cooperates with the HCOPAR. The radio system is operated in HF and VHF bands and determines the tri-coordinate locations of the ionospheric irregularities. Beginning in 2017, software designed radio technology has begun to be applied in the radio system of the WIOBSS family (Qiao L et al., 2017a).

Jiang CH et al. (2016a) presented a new method to reconstruct the vertical electron density profile based on TEC using the simulated annealing algorithm. The Quasi-parabolic segments (QPS) were used to model the bottomside ionosphere. f_0F_2 can be derived from TEC. Moreover, Jiang CH et al. (2017a) developed a software tool named ionoScaler (ionogram Scaler) to carry out manual and automatic scaling of vertical incidence ionograms. The software tool performs well in scaling ionograms and estimation of ITEC.

6. Radio Wave Propagation in the Ionosphere

Zhang XM et al. (2016) studied plasma perturbations induced by high frequency (HF) radio waves. By using experiment results between the DEMETER satellite and SURA heating facility in Russia, they found some common features in plasma parameters at topside ionosphere related to HF radio wave heating process, in which T_e, N_e and N_i (O^+) increase while ions are accelerated upward and cause perturbations in ULF electric field. The authors' simulation results are consistent with DEMETER observations, showing the important role of Ohmic heating and thermal self-focusing instability during HF ionospheric heating.

Gong Y et al. (2017) conducted an analysis of the ratio of negative ions to electron concentration (λ) in the D-region. Previous incoherent scatter radar (ISR) studies have inferred λ without considering the broadening effect that non-thermal fluctuations have on the power spectra. The authors show that the Doppler effect from high frequency non-thermal fluctuations plays a significant role in broadening the ISR power spectra in the lower D-region. The λ inferred in previous ISR studies is likely to be overestimated. Using measured Doppler velocities, the broadening effect on the ISR power spectra due to Doppler shift is eliminated and λ is re-evaluated.

Three Alpha transmitters in Russia are working with the same emitted power of 500 kW and the same radio waves (at 11.9 kHz, 12.6 kHz, and 14.9 kHz), at different positions (KRA at west, NOV in the middle and KHA at the east, respectively). Based on DEMETER records of all these signals, Zhang X et al. (2017) presented electric field spatial distribution features recorded at about 22: 00 local time during the solar minimum in December of 2008. From the KHA transmitter, higher frequency waves can penetrate into the topside ionosphere with higher energy, reaching −70 dB, and can cover much larger longitudinal areas (about 80° at 14.9 kHz). Among the three transmitters, the lowest electric field strength and the smallest longitude scale were detected over KRA, being one order of magnitude lower than the other two transmitters at 11.9 kHz and 12.6 kHz, in which the lower hybrid resonance waves over KRA are seen to affect severely the whistler mode wave propagation. Compared with simulations from the full-wave propagation model, the local ionospheric condition is the controlling factor for wave propagation, where the magnetic field strength and other powerful transmitters at similar frequency can also influence the wave amplitude and their covering areas at different locations.

Zhao SF et al. (2017) constructed a full wave model to estimate the trans-ionospheric absorption of VLF wave, which has been verified with the help of the VLF transmitter. The attenuation of VLF energy waves is mainly in the earth-ionosphere waveguide and the D/E region, which is affected by geomagnetic parameters, ionospheric parameters, and radiation source. When the wave penetrates the D/E region, it turns into whistler mode and propagates along the magnetic force line with small energy attenuation. Zhao SF et al. (2016) found that the D/E region absorption of VLF wave increases with wave frequency, while the attenuation in the waveguide decreases with the increase of the wave frequency in the near field. Variation of the radiation power has no effect on attenuation in the waveguide, nor on D/E region absorption. The absorption in the D/E region decreases with the increase of strength and dip angle of the geomagnetic field, and increases with ionospheric electron density and collision frequency.

Xu X et al. (2016) conducted numerical simulations of the generation and propagation of ultralow-frequency (ULF) waves by artificial ionospheric F region modulation at different latitudes. Their

numerical simulations show the effects of background ionospheric parameters and modulation frequency on the generation and propagation of ULF waves.

Wang X et al.(2016a, b) investigated the parametric instability excited by X-mode heating waves. The parallel electric field of the X-mode heating wave can exceed the threshold of the parametric instability when the heating wave propagates along the magnetic field, and the full dispersion relation of the longitudinal Langmuir wave satisfies the frequency matching condition near the X-mode reflection height. The observed powerful high-frequency (HF)-enhanced ion lines and plasma lines depend on the heating incidence angles. This investigation provides evidence for the existence of a non-Maxwellian distribution of the electrons in the heated region.

Zhou C et al. (2016) present a three-dimensional numerical model of large-scale ionospheric electron density and temperature modulation by powerful electromagnetic waves, by incorporating the transport equations and the three-dimensional ray-tracing algorithm. Thermal processes play important roles in the ionospheric electron density/temperature modulation and large-scale FAI generation.

Acknowledgments

LiBo Liu heartily appreciates many colleagues for kindly providing their articles and pictures for this national report. This report was supported by National Natural Science Foundation of China (41621063, 41774161) and by the Opening Funding of Chinese Academy of Sciences dedicated for the Chinese Meridian Project. Data from the Meridional Project support many works on the report.

References

Chen, G., Wu, C., Zhang, S. D., Ning, B. Q., Huang, X. Q., Zhong, D. K., Qi, H., Wang, J., and Huang, L. (2016a). Midlatitude ionospheric responses to the 2013 SSW under high solar activity. *J. Geophys. Res. Space Phys.*, *121*(1), 790–803. https://doi.org/10.1002/2015JA021980

Chen, G., Cui, X., Chen, F. L., Zhao, Z. Y., Wang, Y., Yao, Q., Wang, C., Lu, D. R., Zhang, S. D., … Gong, W. L. (2016b). MST Radars of Chinese Meridian Project: system description and atmospheric wind measurement. *IEEE Trans. Geosci. Remote Sens.*, *54*(8), 4513–4523. https://doi.org/10.1109/TGRS.2016.2543507

Chen, G., Wang, J., Wu, C., Huang, X. Q., Zhong, D. K., Qi, H., Huang, L., and Li, Y. X. (2016c). Multisite remote sensing for tsunami-induced waves. *IEEE Trans. Geosci. Remote Sens.*, *54*(12), 7177–7184. https://doi.org/10.1109/TGRS.2016.2597165

Chen, G., Jin, H., Yan, J. Y., Zhang, S. D., Li, G. Z., Yokoyama, T., Yang, G T., Yan, C. X., Wu, C., … Wang, Z. H. (2017a). Low-latitude daytime F region irregularities observed in two geomagnetically quiet days by the Hainan coherent scatter phased array radar (HCOPAR). *J. Geophys. Res. Space Phys.*, *122*(2), 2645–2654. https://doi.org/10.1002/2016JA023628

Chen, G., Jin, H., Yan, J. Y., Cui, X., Zhang, S. D., Yan, C. X., Yang, G. T., Lan, A. L., Gong, W. L., … Wang, J. (2017b). Hainan Coherent Scatter Phased Array Radar (HCOPAR): system design and ionospheric irregularity observations. *IEEE Trans. Geosci. Remote Sens.*, *55*(8), 4757–4765. https://doi.org/10.1109/TGRS.2017.2699280

Chen, X. T., Lei, J. H., Wang, W. B., Burns, A. G., Luan, X. L., and Dou, X. K. (2016). A numerical study of nighttime ionospheric variations in the American sector during 28-29 October 2003. *J. Geophys. Res. Space Phys.*, *121*(9), 8985–8994. https://doi.org/10.1002/2016JA023091

Chen, Y. D., Liu, L. B., Le, H. J., Wan, W. X., and Zhang, H. (2016a). Equatorial ionization anomaly in the low-latitude topside ionosphere: Local time evolution and longitudinal difference. *J. Geophys. Res. Space Phys.*, *121*(7), 7166–7182. https://doi.org/10.1002/2016JA022394

Chen, Y. D., Liu, L. B., Le, H. J., Wan, W. X., and Zhang, H. (2016b). The global distribution of the dusk-to-nighttime enhancement of summer N_mF_2 at solar minimum. *J. Geophys. Res. Space Phys.*, *121*(8), 7914–7922. https://doi.org/10.1002/2016JA022670

Chen, Y. D., Liu, L. B., Le, H. J., Wan, W. X., and Zhang, H. (2017). The effect of zonal wind reversal around sunset on ionospheric interhemispheric asymmetry at March equinox of a solar maximum year 2000. *J. Geophys. Res. Space Phys.*, *122*(4), 4726–4735. https://doi.org/10.1002/2017JA023874

Chen, Z., Wang J. S., Deng, X. H., Deng, Y., Huang, C. M., Li, H. M., and Wu, Z. X. (2017a). Study on the relationship between the residual 27 day quasiperiodicity and ionospheric Q disturbances. *J. Geophys. Res. Space Phys.*, *122*(2), 2542–2550. https://doi.org/10.1002/2016JA023195

Chen, Z., Wang, J. S., Deng, Y., and Huang, C. M. (2017b). Extraction of the geomagnetic activity effect from TEC data: A comparison between the spectral whitening method and 28 day running median. *J. Geophys. Res. Space Phys.*, *122*(3), 3632–3639. https://doi.org/10.1002/2016JA023412

Cui, X., Chen, G., Wang, J., Song, H., and Gong, W. L. (2016). Design and application of Wuhan ionospheric oblique backscattering sounding system with the addition of an antenna array (WIOBSS-AA). *Sensors*, *16*(6), 887. https://doi.org/10.3390/s16060887

Dang, T., Luan, X. L., Lei, J. H., Dou, X. K., and Wan, W. X. (2016). A numerical study of the interhemispheric asymmetry of the equatorial ionization anomaly in solstice at solar minimum. *J. Geophys. Res. Space Phys.*, *121*(9), 9099–9110. https://doi.org/10.1002/2016JA023012

Dang, T., Wang, W. B., Burns, A., Dou, X. K., Wan, W. X., and Lei, J. H. (2017). Simulations of the ionospheric annual asymmetry: Sun-Earth distance effect. *J. Geophys. Res. Space Phys.*, *122*(6), 6727–6736. https://doi.org/10.1002/2017JA024188

Ding, F., Mao, T., Hu, L. H., Ning, B. Q., Wan, W. X., and Wang, Y. G. (2016). GPS network observation of traveling ionospheric disturbances following the Chelyabinsk meteorite blast. *Ann. Geophys.*, *34*(11), 1045–1051. https://doi.org/10.5194/angeo-34-1045-2016

Gong, Y., Zhou, Q. H., and Zhang, S. D. (2016a). A study on electric field mapping from the F region to the E region at Arecibo. *J. Geophys. Res. Space Phys.*, *121*(1), 713–718. https://doi.org/10.1002/2015JA022035

Gong, Y., Zhou, Q. H., Zhang, S. D., Aponte, N., and Sulzer, M. (2016b). An incoherent scatter radar study of the midnight temperature maximum that occurred at Arecibo during a sudden stratospheric warming event in January 2010. *J. Geophys. Res. Space Phys.*, *121*(6), 5571–5578. https://doi.org/10.1002/2016JA022439

Gong, Y., Ma, Z., Li, Y. L., Zhou, Q. H., Zhang, S. D., and Huang, C. M. (2017). The effect of Doppler broadening on D region negative ion ratio measurements at Arecibo. *J. Geophys. Res. Space Phys.*, *122*(5), 5816–5824. https://doi.org/10.1002/2016JA023805

Hao, Y. Q., Huang, J. P., Liu, W. L., Zhang, D. H., and Xiao, Z. (2017). Prompt GPS TEC response to magnetospheric compression. *J. Geophys. Res. Space Phys.*, *122*(4), 4357–4366. https://doi.org/10.1002/2017JA023866

He, F., Zhang, X. X., Wang, W. B., and Chen, B. (2016). Double-peak subauroral ion drifts (DSAIDs). *Geophys. Res. Lett.*, *43*(11), 5554–5562. https://doi.org/10.1002/2016GL069133

He, F., Zhang, X. X., Wang, W. B., and Wan, W. X. (2017). Different evolution patterns of subauroral polarization streams (SAPS) during intense storms and quiet time substorms. *Geophysical Research Letters*, *44*(21), 10796–10804. https://doi.org/10.1002/2017GL075449

Hu, L. H., Yue, X. A., and Ning, B. Q. (2017). Development of the Beidou Ionospheric Observation Network in China for space weather monitoring. *Space Wea.*, *15*(8), 974–984. https://doi.org/10.1002/2017SW001636

Huang, F. Q., Dou, X. K., Lei, J. H., Lin, J., Ding, F., and Zhong, J. H. (2016). Statistical analysis of nighttime medium-scale traveling ionospheric disturbances using airglow images and GPS observations over central China. *J. Geophys. Res. Space Phys.*, *121*(9), 8887–8899.

https://doi.org/10.1002/2016JA022760

Huang, F. Q., Lei, J. H., and Dou, X. K. (2017). Daytime ionospheric longitudinal gradients seen in the observations from a regional BeiDou GEO receiver network. *J. Geophys. Res. Space Phys.*, *122*(6), 6552–6561. https://doi.org/10.1002/2017JA023881

Huang, H., Liu, L. B., Chen, Y. D., Le, H. J., and Wan, W. X. (2016). A global picture of ionospheric slab thickness derived from GIM TEC and COSMIC radio occultation observations. *J. Geophys. Res. Space Phys.*, *121*(1), 867–880. https://doi.org/10.1002/2015JA021964

Jiang, C. H., Yang, G. B., Zhu, P., Nishioka, M., Yokoyama, T., Zhou, C., Song, H., Lan, T., Zhao, Z. Y., and Zhang, Y. N. (2016a). Reconstruction of the vertical electron density profile based on vertical TEC using the simulated annealing algorithm. *Adv. Space Res.*, *57*(10), 2167–2176. https://doi.org/10.1016/j.asr.2016.02.020

Jiang, C. H., Deng, C., Yang, G. B., Liu, J., Zhu, P., Yokoyama, T., Song, H., Lan, T., Zhou, C., … Yatini C. Y. (2016b). Latitudinal variation of the specific local time of postmidnight enhancement peaks in F layer electron density at low latitudes: A case study. *J. Geophys. Res. Space Phys.*, *121*(4), 3476–3483. https://doi.org/10.1002/2015JA022319

Jiang, C. H., Yang, G. B., Liu, J., Yokoyama, T., Komolmis, T., Song, H., Lan, T., Zhou, C., Zhang, Y. N., and Zhao, Z. Y. (2016c). Ionosonde observations of daytime spread F at low latitudes. *J. Geophys. Res. Space Phys.*, *121*(12), 12093–12103. https://doi.org/10.1002/2016JA023123

Jiang, C. H., Yang, G. B., Zhou, Y., Zhu, P., Lan, T., Zhao, Z. Y., and Zhang, Y. N. (2017a). Software for scaling and analysis of vertical incidence ionograms-ionoScaler. *Adv. Space Res.*, *59*(4), 968–979. https://doi.org/10.1016/j.asr.2016.11.019

Jiang, C. H., Yang, G. B., Liu, J., Yokoyama, T., Liu, T. X., Lan, T., Zhou, C., Zhang, Y. N., Zhao, Z. Y., … Yatini, C. Y. (2017b). Equatorial and low-latitude ionospheric response to the 17-18 March 2015 great storm over Southeast Asia longitude sector. *J. Geophys. Res. Space Phys.*, *122*(5), 5756–5767. https://doi.org/10.1002/2017JA024134

Kuai, J. W., Liu, L. B., Liu, J., Sripathi, S., Zhao, B. Q., Chen, Y. D., Le, H. J., and Hu, L. H. (2016). Effects of disturbed electric fields in the low-latitude and equatorial ionosphere during the 2015 St. *Patrick's Day storm. J. Geophys. Res. Space Phys.*, *121*(9), 9111–9126. https://doi.org/10.1002/2016JA022832

Kuai, J. W., Liu, L. B., Lei, J. H., Liu, J., Zhao, B. Q., Chen, Y. D., Le, H. J., Wang, Y. G., and Hu, L. H. (2017). Regional differences of the ionospheric response to the July 2012 geomagnetic storm. *J. Geophys. Res. Space Phys.*, *122*(4), 4654–4668. https://doi.org/10.1002/2016JA023844

Le, H. J., Liu, L. B., Ren, Z. P., Chen, Y. D., Zhang, H., and Wan, W. X. (2016a). A modeling study of global ionospheric and thermospheric responses to extreme solar flare. *J. Geophys. Res. Space Phys.*, *121*(1), 832–840. https://doi.org/10.1002/2015JA021930

Le, H. J., Liu, L. B., Ren, Z. P., Hu, L. H., Chen, Y. D., and Wan, W. X. (2016b). An ionospheric assimilation model along a meridian plane. *J. Atmos. Solar Terr. Phys.*, *145*, 125–135. https://doi.org/10.1016/j.jastp.2016.05.003

Le, H. J., Yang, N., Liu, L. B., Chen, Y. D., and Zhang, H. (2017). The latitudinal structure of nighttime ionospheric TEC and its empirical orthogonal functions model over North American sector. *J. Geophys. Res. Space Phys.*, *122*(1), 963–977. https://doi.org/10.1002/2016JA023361

Lei, J. H., Wang, W. B., Burns, A. G., Luan, X. L., and Dou, X. K. (2016a). Can atomic oxygen production explain the ionospheric annual asymmetry?. *J. Geophys. Res. Space Phys.*, *121*(7), 7238–7244. https://doi.org/10.1002/2016JA022648

Lei, J. H., Zhong, J. H., Mao, T., Hu, L. H., Yu, T., Luan, X. L., Dou, X. K., Sutton, E., Yue, X. A., … Batista, I. S. (2016b). Contrasting behavior of the F_2 peak and the topside ionosphere in response to the 2 October 2013 geomagnetic storm. *J. Geophys. Res. Space Phys.*, *121*(10), 10549–10563. https://doi.org/10.1002/2016JA022959

Li, G. Z., Otsuka, Y., Ning, B. Q., Abdu, M. A., Yamamoto, M., Wan, W. X., Liu, L. B., and Abadi, P. (2016). Enhanced ionospheric plasma bubble generation in more active ITCZ. *Geophys. Res. Lett.*, *43*(6), 2389–2395. https://doi.org/10.1002/2016GL068145

Li, G. Z., Ning, B. Q., Abdu, M. A., Wan, W. X., Wang, C., Yang, G. T., Liu, K. K., Liu, L. B., and Yan, C. X. (2017). First observation of presunset ionospheric F region bottom-type scattering layer. *J. Geophys. Res. Space Phys.*, *122*(3), 3788–3797. https://doi.org/10.1002/2016JA023647

Li, M., Yuan, Y. B., Wang, N. B., Liu, T., and Chen, Y. C. (2017a). Estimation and analysis of the short-term variations of multi-GNSS receiver differential code biases using global ionosphere maps. *J. Geodesy*. https://doi.org/10.1007/s00190-017-1101-3

Li, M., Yuan, Y. B., Zhang, B. C., Wang, N. B., Li, Z. S., Liu, X. F., and Zhang, X. (2017b). Determination of the optimized single-layer ionospheric height for electron content measurements over China. *J. Geodesy*, *92*(2), 169–183. https://doi.org/10.1007/s00190-017-1054-6

Liu, H. T., Ding, F., Zhao, B. Q., Li, J. Y., Hu, L. H., Wan, W. X., and Ning, B. Q. (2017). Ionospheric response following the M_w 7.8 Gorkha earthquake on 25 April 2015. *J. Geophys. Res. Space Phys.*, *122*(6), 6495–6507. https://doi.org/10.1002/2016JA023079

Liu, J., Jiang, C. H., Deng, C., Yang, G. B., Zhang, X. M., Lou, W. Y., and Yang, C. H. (2016a). Vertical ionosonde net and its data application in southwestern China. *Acta Seismol. Sin.* (*in Chinese*), *38*(3), 399–407. https://doi.org/10.11939/jass.2016.03.007

Liu, J., Lou, W. Y., Zhang, X. M., and Shen, X. H. (2016b). A comparison study of foF2 derived from oblique sounding network and vertical ionosonde in Northern China. *Terr. Atmos. Ocean Sci.*, *27*(6), 933–941. https://doi.org/10.3319/TAO.2016.03.06.01(AA)

Liu, J., Zhang, X. M., Novikov, V., and Shen, X. H. (2016c). Variations of ionospheric plasma at different altitudes before the 2005 Sumatra Indonesia M_s 7.2 earthquake. *J. Geophys. Res. Space Phys.*, *121*(9), 9179–9187. https://doi.org/10.1002/2016JA022758

Liu, L. B., and Wan, W. X. (2016). New understanding achieved from 2 years of Chinese ionospheric Investigations. *Sci. Bull.*, *61*(7), 524–542. https://doi.org/10.1007/s11434-016-1035-9

Luan, X. L., Lei, J. H., Dou, X. K., and Dang, T. (2016). Double crests of peak height in the equatorial ionospheric F_2 layer observed by COSMIC. *J. Geophys. Res. Space Phys.*, *121*(1), 529–537. https://doi.org/10.1002/2015JA021611

Ma, Z., Yun, G., Zhang, S. D., Zhou, Q. H., Huang, C. M., Huang, K. M., Yu, Y., Li, G. Z., Ning, Q. Q., and Li, C. (2017). Responses of quasi 2 day waves in the MLT region to the 2013 SSW revealed by a meteor radar chain. *Geophys. Res. Lett.*, *44*(18), 9142–9150. https://doi.org/10.1002/2017GL074597

Ouyang, X. Y., Liu, W. L., Xiao, Z., and Hao, Y. Q. (2016). Observations of ULF waves on the ground and ionospheric Doppler shifts during Storm Sudden Commencement. *J. Geophys. Res. Space Phys.*, *121*(4), 2976–2983. https://doi.org/10.1002/2015JA022092

Priyadarshi, S., Zhang, Q. H., Ma, Y. Z., Wang, Y., and Xing, Z. Y. (2016). Observations and modeling of ionospheric scintillations at South Pole during six X-class solar flares in 2013. *J. Geophys. Res. Space Phys.*, *121*(6), 5737–5751. https://doi.org/10.1002/2016JA022833

Qiao, L., Chen, G., Cui, X., and Gong, W. L. (2017a). Comparison of the traditional ionosonde and the digital ionosonde based on direct digitization. *IEEE Geosci. Remote Sens. Lett.*, *14*(2), 198–202. https://doi.org/10.1109/LGRS.2016.2634082

Qiao, L., Chen, G., and Wang, J. (2017b). Design and application of the distributed ionospheric coherent scatter radar. *IEEE Geosci. Remote Sens. Lett.*, *14*(11), 2042–2046. https://doi.org/10.1109/LGRS.2017.2749605

Ren, D. X., and Lei, J. H. (2017). A simulation study of the equatorial ionospheric response to the October 2013 geomagnetic storm. *J. Geophys. Res. Space Phys.*, *122*(9), 9696–9704. https://doi.org/10.1002/2017JA024286.

She, C. L., Wan, W. X., Yue, X. A., Xiong, B., Yu, Y., Ding, F., and Zhao B. Q. (2017). Global ionospheric electron density estimation based on multisource TEC data assimilation. *GPS Solut.*, *21*(3), 1125–1137. https://doi.org/10.1007/s10291-016-0580-7

Shen, X. H., and Zhang, X. M. (2017). The spatial distribution of hydrogen ions at topside ionosphere in local daytime. *Terr. Atmos. Ocean. Sci.*, *28*(6), 1009–1017. https://doi.org/10.3319/TAO.2017.06.30.01

Shen, X. H., Zhima, Z., Zhao, S. F., Qian, G., Ye, Q., and Ruzhin, Y. (2017). VLF radio wave anomalies associated with the 2010 Ms 7.1 Yushu earthquake. *Adv. Space Res.*, *59*(10), 2636–2644. https://doi.org/10.1016/j.asr.2017.02.040

Song, Q., Ding, F., Zhang, X. X., and Mao, T. (2017). GPS detection of the ionospheric disturbances over China due to impacts of Typhoons Rammasum and Matmo. *J. Geophys. Res. Space Phys.*, *122*(1), 1055–1063.

https://doi.org/10.1002/2016JA023449

Wang, X., Cannon, P., Zhou, C., Honary, F., Ni, B. B., and Zhao, Z. Y. (2016a). A theoretical investigation on the parametric instability excited by X-mode polarized electromagnetic wave at Tromsø. *J. Geophys. Res. Space Phys.*, *121*(4), 3578–3591. https://doi.org/10.1002/2016JA022411

Wang, X., Zhou, C., Liu, M. R., Honary, F., Ni, B. B., and Zhao, Z. Y. (2016b). Parametric instability induced by X-mode wave heating at EISCAT. *J. Geophys. Res. Space Phys.*, *121*(10), 10536–10548. https://doi.org/10.1002/2016JA023070

Wang, Y., Zhang, Q. H., Jayachandran, P. T., Lockwood, M., Zhang, S. R., Moen, J., Xing, Z. Y., Ma, Y. Z., and Lester, M. (2016). A comparison between large-scale irregularities and scintillations in the polar ionosphere. *Geophys. Res. Lett.*, *43*(10), 4790–4798. https://doi.org/10.1002/2016GL069230

Xiong, B., Wan, W. X., Yu, Y., and Hu, L. H. (2016). Investigation of ionospheric TEC over China based on GNSS data. *Adv. Space Res.*, *58*(6), 867–877. https://doi.org/10.1016/j.asr.2016.05.033

Xu, X., Zhou, C., Shi, R., Ni, B. B., Zhao, Z. Y., and Zhang, Y. N. (2016). Numerical study of the generation and propagation of ultralow-frequency waves by artificial ionospheric F region modulation at different latitudes. *Ann. Geophys.*, *34*(9), 815–829. https://doi.org/10.5194/angeo-34-815-2016

Xue, X. H., Li, G. Z., Dou, X. K., Yue, X. A., Yang, G. T., Chen, J. S., Chen, T. D., Ning, B. Q., Wang, J. H., … Wan, W. X. (2017). An overturning-like thermospheric Na layer and its relevance to Ionospheric field aligned irregularity and sporadic E. *J. Atmos. Solar Terr. Phys.*, *162*, 151–161. https://doi.org/10.1016/j.jastp.2016.12.006

Yan, X. X., Yu, T., Shan, X. J., and Xia, C. L. (2017). Ionospheric TEC disturbance study over seismically region in China. *Adv. Space Res.*, *60*(12), 2822–2835. https://doi.org/10.1016/j.asr.2016.12.004

Yang, C. J., Zhao, B. Q., Zhu, J., Yue, X. A., and Wan, W. X. (2017). An investigation of ionospheric upper transition height variations at low and equatorial latitudes deduced from combined COSMIC and C/NOFS measurements. *Adv. Space Res.*, *60*(8), 1617–1628. https://doi.org/10.1016/j.asr.2016.11.024

Yang, N., Le, H. J., and Liu, L. B. (2016). Statistical analysis of the mid-latitude trough position during different categories of magnetic storms and different storm intensities. *Earth Planets Space*, *68*(1), 171. https://doi.org/10.1186/s40623-016-0554-6

Yu, B. K., Xue, X. H., Lu, G. P., Ma, M., Dou, X. K., Qie, X. S., Ning, B. Q., Hu, L. H., Wu, J. F., and Chi, Y. T. (2015). Evidence for lightning-associated enhancement of the ionospheric sporadic E layer dependent on lightning stroke energy. *J. Geophys. Res. Space Phys.*, *120*(10), 9202–9212. https://doi.org/10.1002/2015JA021575

Yu, S. M., Xiao, Z., Aa, E., Hao, Y. Q., and Zhang, D. H. (2016a). Observational investigation of the possible correlation between medium-scale TIDs and mid-latitude spread F. *Adv. Space Res.*, *58*(3), 349–357. https://doi.org/10.1016/j.asr.2016.05.002

Yu, S. M., Xiao, Z., Zhao, B. Q., Zhang, D. H., and Hao, Y. Q. (2016b). Longitudinal difference in total electron content over the East Asian region: Feature and explanation. *J. Atmos. Solar Terr. Phys.*, *148*, 74–81. https://doi.org/10.1016/j.jastp.2016.08.015

Yu, T., Xia, C. L., Zuo, X. M., Huang, C., Mao, T., Liu, L. B., and Liu, Z. Z. (2016). A comparison of mesospheric and low-thermospheric winds measured by Fabry-Perot interferometer and meteor radar over central China. *J. Geophys. Res. Space Phys.*, *121*(10), 10037–10051. https://doi.org/10.1002/2016JA022997

Yu, T., Zuo, X. M., Xia, C. L., Li, M. Y., Huang, C., Mao, T., Zhang, X. X., Zhao, B. Q., and Liu, L. B. (2017). Peak height of OH airglow derived from simultaneous observations a Fabry-Perot interferometer and a meteor radar. *J. Geophys. Res. Space Phys.*, *122*(4), 4628–4637. https://doi.org/10.1002/2016JA023743

Yue, X. A., Schreiner, W. S., Pedatella, N. M., and Kuo, Y. H. (2016a). Characterizing GPS radio occultation loss of lock due to ionospheric weather. *Space Wea.*, *14*(4), 285–299. https://doi.org/10.1002/2015SW001340

Yue, X. A., Wang, W. B., Lei, J. H., Burns, A., Zhang, Y. L., Wan, W. X., Liu, L. B., Hu, L. H., Zhao, B. Q., and Schreiner, W. S. (2016b). Long-lasting negative ionospheric storm effects in low and middle latitudes during the recovery phase of the 17 March 2013 geomagnetic storm. *J. Geophys. Res. Space Phys.*, *121*(9), 9234–9249. https://doi.org/10.1002/2016JA022984

Yue, X. N., Wan, W. X., Liu, L. B., Liu, J., Zhang, S. R., Schreiner, W. S., Zhao, B. Q., and Hu, L. H. (2016). Mapping the conjugate and corotating storm-enhanced density during 17 March 2013 storm through data assimilation. *J. Geophys. Res. Space Phys.*, *121*(12), 12202–12210. https://doi.org/10.1002/2016JA023038

Zhang, B. C., Teunissen, P. J. G., Yuan, Y. B., Zhang, H. X., and Li, M. (2017). Joint estimation of vertical total electron content (VTEC) and satellite differential code biases (SDCBs) using low-cost receivers. *J. Geodesy*, *92*(4), 401–413. https://doi.org/10.1007/s00190-017-1071-5

Zhang, M. L., Liu, L. B., Wan, W. X., and Ning, B. Q. (2017). Comparison of the observed topside ionospheric and plasmaspheric electron content derived from the COSMIC podTEC measurements with the IRI_Plas model results. *Adv. Space Res.*, *60*(2), 222–227. https://doi.org/10.1016/j.asr.2016.10.025

Zhang, Q. H., Zong, Q. G., Lockwood, M., Heelis, R. A., Hairston, M., Liang, J., McCrea, I., Zhang, B. C., Moen, J., … Ma, Y. Z. (2016a). Earth's ion upflow associated with polar cap patches: Global and in situ observations. *Geophys. Res. Lett.*, *43*(5), 1845–1853. https://doi.org/10.1002/2016GL067897

Zhang, Q. H., Moen, J., Lockwood, M., McCrea, I., Zhang, B. C., McWilliams, K. A., Zong, Q. G., Zhang, S. R., Ruohoniemi, J. M., … Lester, M. (2016b). Polar cap patch transportation beyond the classic scenario. *J. Geophys. Res. Space Phys.*, *121*(9), 9063–9074. https://doi.org/10.1002/2016JA022443

Zhang, Q. H., Ma, Y. Z., Jayachandran, P. T., Moen, J., Lockwood, M., Zhang, Y. L., Foster, J. C., Zhang, S. R., Wang, Y., … Xing, Z. Y. (2017). Polar cap hot patches: Enhanced density structures different from the classical patches in the ionosphere. *Geophys. Res. Lett.*, *44*(16), 8159–8167. https://doi.org/10.1002/2017GL073439

Zhang, R. L., Liu, L. B., Chen, Y. D., and Le, H. J. (2015). The dawn enhancement of the equatorial ionospheric vertical plasma drift. *J. Geophys. Res. Space Phys.*, *120*(12), 10688–10697. https://doi.org/10.1002/2015JA021972

Zhang, R. L., Liu, L. B., Le, H. J., and Chen, Y. D. (2016). Evidence and effects of the sunrise enhancement of the equatorial vertical plasma drift in the F region ionosphere. *J. Geophys. Res. Space Phys.*, *121*(5), 4826–4834. https://doi.org/10.1002/2016JA022491

Zhang, R. L., Liu, L. B., Le, H. J., and Chen, Y. D. (2017a). Equatorial ionospheric electrodynamics during solar flares. *Geophys. Res. Lett.*, *44*(10), 4558–4565. https://doi.org/10.1002/2017GL073238

Zhang, R. L., Liu, L. B., Le, H. J., Chen, Y. D., and Kuai, J. W. (2017b). The storm time evolution of the ionospheric disturbance plasma drifts. *J. Geophys. Res. Space Phys.*, *122*(11), 11665–11676. https://doi.org/10.1002/2017JA024637

Zhang, X., Zhao, S. F., Ruzhin, Y., Liu, J., and Song, R. (2017). The spatial distribution features of three Alpha transmitter signals at the topside ionosphere. *Radio Sci.*, *52*(5), 653–662. https://doi.org/10.1002/2016RS006219

Zhang, X. F., Liu, L. B., and Liu, S. T. (2017). Dependence of thermospheric zonal winds on solar flux, geomagnetic activity, and hemisphere as measured by CHAMP. *J. Geophys. Res. Space Phys.*, *122*(8), 8893–8914. https://doi.org/10.1002/2016JA023715

Zhang, X. M., Frolov, V., Zhou, C., Zhao, S. F., Ruzhin, Y., Shen, X. H., Zhima, Z., and Liu, J. (2016). Plasma perturbations HF-induced in the topside ionosphere. *J. Geophys. Res. Space Phys.*, *121*(10), 10052–10063. https://doi.org/10.1002/2016JA022484

Zhao, S. F., Liao, L., Zhang, X. M., and Shen, X. H. (2016). Full wave calculation of ground-based VLF radiation penetrating into the ionosphere. *Chin. J. Radio Sci.* (*in Chinese*), *31*(5), 825–833. https://doi.org/10.13443/j.cjors.2016021701

Zhao, S. F., Liao, L., and Zhang, X. M. (2017). Trans-ionospheric VLF wave power absorption of terrestrial VLF signal. *Chin. J. Geophys.* (*in Chinese*), *60*(8), 3004–3014. https://doi.org/10.6038/cjg20170809

Zhao, X. K., Ning, B. Q., Zhang, M. L., and Hu, L. H. (2017). Comparison of the ionospheric F2 peak height between ionosonde measurements and IRI2016 predictions over China. *Adv. Space Res.*, *60*(7), 1524–1531. https://doi.org/10.1016/j.asr.2017.06.056

Zhima, Z., Chen, L. J., Xiong, Y., Cao, J. B., and Fu, H. S. (2017). On the origin of ionospheric hiss: a conjugate observation. *J. Geophys. Res. Space Phys.*,

122(11), 11784–11793. https://doi.org/10.1002/2017JA024803

Zhong, J. H., Lei, J. H., Yue, X. A., and Dou, X. K. (2016a). Determination of differential code bias of GNSS receiver onboard low Earth orbit satellite. *IEEE Trans. Geosci. Remote Sens.*, *54*(8), 4896–4905. https://doi.org/10.1109/TGRS.2016.2552542

Zhong, J. H., Wang, W. B., Yue, X. A., Burns, A. G., Dou, X. K., and Lei, J. H. (2016b). Long-duration depletion in the topside ionospheric total electron content during the recovery phase of the March 2015 strong storm. *J. Geophys. Res. Space Phys.*, *121*(5), 4733–4747. https://doi.org/10.1002/2016JA022469

Zhong, J. H., Lei, J. H., Wang, W. B., Burns, A. G., Yue, X. A., and Dou, X. K. (2017). Longitudinal variations of topside ionospheric and plasmaspheric TEC. *J. Geophys. Res. Space Phys.*, *122*(7), 6737–6760. https://doi.org/10.1002/2017JA024191

Zhou, C., Ni, B. B., Wang, X., Liu, M. R., Xu, X., Wang, C., Shi, R., Gu, X. D., Zhang, Y. N., and Zhao, Z. Y. (2016). A numerical study of large-scale ionospheric modulation due to the thermal process by powerful wave heating. *J. Geophys. Res. Space Phys.*, *121*(3), 2704–2714. https://doi.org/10.1002/2016JA022355

Zhou, C., Liu, Y., Zhao, S. F., Liu, J., Zhang, X. M., Huang, J. P., Shen, X. H., Ni, B. B., and Zhao, Z. Y. (2017a). An electric field penetration model for seismo-ionospheric research. *Adv. Space Res.*, *60*(10), 2217–2232. https://doi.org/10.1016/j.asr.2017.08.007

Zhou, C., Tang, Q., Song, X. X., Qing, H. Y., Liu, Y., Wang, X., Gu, X. D., Ni, B. B., and Zhao, Z. Y. (2017b). A statistical analysis of sporadic E layer occurrence in the midlatitude China region. *J. Geophys. Res. Space Phys.*, *122*(3), 3617–3631. https://doi.org/10.1002/2016JA023135

Zhou, S., Luan, X. L., and Dou, X. K. (2016). Solar activity dependence of nightside aurora in winter conditions. *J. Geophys. Res. Space Phys.*, *121*(2), 1619–1626. https://doi.org/10.1002/2015JA021865

Zhou, Y. L., Lühr, H., Alken, P., and Xiong, C. (2016a). New perspectives on equatorial electrojet tidal characteristics derived from the Swarm constellation. *J. Geophys. Res. Space Phys.*, *121*(7), 7226–7237. https://doi.org/10.1002/2016JA022713

Zhou, Y. L., Wang, L., Xiong, C., Lühr, H., and Ma, S. Y. (2016b). The solar activity dependence of nonmigrating tides in electron density at low and middle latitudes observed by CHAMP and GRACE. *Ann. Geophys.*, *34*(4), 463–472. https://doi.org/10.5194/angeo-34-463-2016.

Zhu, Q. Y., Lei, J. H., Luan, X. L., and Dou, X. K. (2016). Contribution of the topside and bottomside ionosphere to the total electron content during two strong geomagnetic storms. *J. Geophys. Res. Space Phys.*, *121*(3), 2475–2488. https://doi.org/10.1002/2015JA022111

Zuo, X., Yu, T., Xia, C., Huang, J., and Xu, J. (2016). Coordinated study of scintillations recorded by Chinese FY-2 geostationary meteorological satellite and VHF coherent radar observations over south China. *J. Atmos. Solar Terr. Phys.*, *147*, 41–49. https://doi.org/10.1016/j.jastp.2016.06.012